International Journal of Mechanical Sciences 232 (2022) 107571

Contents lists available at ScienceDirect

International Journal of Mechanical Sciences

journal homepage: www.elsevier.com/locate/ijmecsci

Investigating the relationship of hardness and flow stress in metal forming

André Rudnytskyj [a,b,*], Markus Varga [a], Stefan Krenn [a], Georg Vorlaufer [a], Josef Leimhofer [c], Martin Jech [a], Carsten Gachot [b]

[a] AC2T research GmbH, Viktor-Kaplan-Straße 2/C, Wiener Neustadt, 2700, Austria
[b] TU Wien, Institute of Engineering Design and Product Development, Lehárgasse 6, Objekt 7 (Hoftrakt BD, Campus Getreidemarkt), Vienna, 1060, Austria
[c] AMAG rolling GmbH, Lamprechtshausener Straße 61, Ranshofen, 5282, Austria

ARTICLE INFO

Keywords:
High temperature hardness
Aluminium alloys
Flow stress
Thermo-viscoplasticity
Finite Element analysis
Metal forming

ABSTRACT

Hardness is routinely utilised to link the bulk material properties to surface contact mechanics. Besides possible differences in the material properties between bulk and surface, there is no established relation between hardness and the thermo-viscoplastic flow stress of materials used in the context of metal forming processes. The purpose of this study is to investigate such relationship using 6061 and 6016 aluminium alloys manufactured by hot rolling. Optical microscopy and Vickers hardness tests at different loads and temperatures ranging from 22 °C up to 450 °C were carried out. A time-dependent Finite Element model of an indentation using thermo-viscoplastic material model based on bulk samples was developed and compared with experiments. Overall, no significant difference between bulk and surface for neither alloy was experimentally identified. The hardness decrease with temperature of the alloys is quantified and ready-to-use constraint factor maps associating the thermo-viscoplastic flow stress with hardness of the materials are presented. The numerical model allowed visualisation of viscoplastic effects, whereas comparisons to the experiments in terms of hardness and topography validated the model and constitutive equations. Constitutive equations derived from compression tests of bulk samples can confidently describe deformation at the surface level and so, be used to develop a contact model in the tribological context of metal forming.

1. Introduction

Hardness is routinely associated with the yield stress of a material and has important applications. The review by Hutchings [1] reports on how the uses, experiments, and investigations of indentation hardness in the first half of the 20th century paved the way for Tabor [2,3] to build up a theoretical basis and study the relationship between yield stress and hardness. As Tabor wrote [2], a hard indenter pressed on a relatively softer metal specimen will reach *full* plastic conditions when the mean pressure, i.e., load divided by the projected area of the indentation, reaches a value of 2.6 to 3 times the yield stress, σ_y, of the softer material. By "full plastic conditions", it is meant that the mean pressure varies little with further increase in indentation size, such that it becomes independent from the load and proportional to the yield stress. Therefore, the mean contact pressure over a fully plastic indentation, i.e., the *indentation hardness*, H, is expressed in terms of yield stress of the material as

$$H = c\sigma_y \tag{1}$$

where c, named "constraint factor", varies between 2.6 and 3 for metals (for aluminium, the value 2.8 is reported by Tabor [2]).

Eq. (1) has been extensively studied at room temperature and with regards to strain hardening. Verifications [4–7], and modifications [8–10] have been reported in the literature; recent examples, include investigations at room temperature on cohesive-frictional materials [11], use of the slip line theory [12], and a discussion on the generality of such relationships [13]. Overall, there is no universal consensus, but the expression can be said to be generally true for severely cold worked metal, which essentially do not work harden. In work-hardening metals, a "representative strain" in terms of the size of the indentation can be used, such that the proportionality of Eq. (1) remains valid. For Vickers hardness, for example, H should result in $\approx c\sigma_y(0.08)$, where $\sigma_y(0.08)$ is the yield stress of the material at a strain of 0.08, taken from a stress–strain curve of a tensile test [2].

Hardness is particularly important in contact mechanics involving plasticity. By assuming that the contact between two solid bodies occurs at the tip of surface asperities, Bowden and Tabor [14,15] further proposed that such contacts would resemble an indentation in the softer material in order to support the external load or imposed displacement. As a result, hardness would define the *real contact area*, which greatly

* Corresponding author at: AC2T research GmbH, Viktor-Kaplan-Straße 2/C, Wiener Neustadt, 2700, Austria.
E-mail address: andre.rudnytskyj@ac2t.at (A. Rudnytskyj).

https://doi.org/10.1016/j.ijmecsci.2022.107571
Received 3 May 2022; Received in revised form 8 July 2022; Accepted 24 July 2022
Available online 29 July 2022

defines friction, particularly in metal forming process [16–20] where it consequently affects the energy consumption in the process. In this sense, hardness can be seen as the initial step to investigate friction and wear in tribological problems [21–25]. The reasoning by Bowden and Tabor for the contact area assumes H is well defined by the constraint factor and the yield stress of the material, but one might question if such relation also applies for materials under metal forming conditions. In hot rolling of certain aluminium alloys, for example, not only strain hardening, but also time- and temperature-dependent material properties are playing a role in the *flow stress* (the true stress that causes further plastic deformation) of the material.

Changes in the deformation due to temperature evidently affects hardness [26,27], but it is unclear how the constraint factor is affected. In ferritic steels, Hsu [28] reported that such changes could separate hardness dependence on temperature into two linear regions, which would suggest that relation (1) is not true for large span of temperature, but rather for limited ranges. High temperature hardness has been studied in the past [29–34] and the literature shows hardness generally decreases with temperature, but that there is no universal conclusion on the specifics of this dependence [35]. In the context of metal forming, the constraint factor is still commonly used according to Tabor as 2.6-3, e.g., in sheet metal forming [36,37], and rolling of steels [18], for calculations of the contact area and friction. Nonetheless, the conditions of thermo-viscoplasticity of the deforming material in such processes significantly change the flow stress and whether usual values of constraint factor are still valid is often overlooked. In the methodology for calculation of contact area proposed by [17,38] and adapted in [39], the contact pressure, i.e., hardness, is individually obtained for each contacting micro-region by means of a Finite Element (FE) simulations. Such methodology may require long computational times since it involves several simulations, but it allows specific conditions such as creep to be looked at in individual asperities [40]. While this approach avoids the use of Eq. (1), there is still a need to verify if the constitutive relations of the material model (which are normally built based on experiments using bulk samples of the material) can properly describe the material properties at the surface level. Korzekwa et al. [41] investigated the viscoplastic flattening of asperities in sheet forming and based the contact pressure on the bulk flow stress to analyse the growth of the contact area. However, different features at the surface such as, for example, a work hardened zone or a thin coating will lead to surface properties different from those of the bulk [42].

Investigations considering temperature and time-dependent properties are not so straight-forward. Kumaraswamy et al. [43,44] separately studied the effects of temperature based on static hardness and the effects of strain rate using dynamic indentation tests with projectiles for titanium alloys, but no discussion was presented regarding temperature or representative values of strain or strain rate for the flow stress calculation. With regards to aluminium, hardness and thermo-mechanical processing of certain aluminium alloys have been studied in particular situations [45–48], but not in a thermo-viscoplastic metal forming context. The use of numerical methods has also been explored and elucidated new discussions [10,49–51], including investigations on the constraint factor; Stone and Elmustafa [52] e.g., briefly write that the strain rate sensitivity of nanoindentation hardness differs from that of the flow stress, but lack experimental comparisons. Recently, Hamada et al. [53] re-examined the constraint factor correlation studying work-hardening in steels, while Zhang et al. [54] investigated the relation between high temperature indentations and compression tests, but in a quasi-static context.

In view of the available literature, there is a clear need for further research on the relationship of thermo-viscoplastic flow stress and hardness in the metal forming context. Thus, this work proposes to investigate the surface material properties of aluminium alloys manufactured by hot rolling and how they relate with their bulk properties, for the purpose of developing an accurate contact model for metal forming processes. To achieve this goal, room temperature (RT) and high temperature (HT) Vickers hardness tests are performed to investigate any difference between bulk and surface regions of two aluminium alloys, namely a 6061 and a 6016. The HT tests further allow to quantify and study the change in hardness with temperature. Experimental flow curves from compression tests of bulk samples are used for building constitutive equations used in a time-dependent FE Vickers indentation model. The hardness and size of the indentations are compared between model and experiments, allowing an independent investigation of whether constitutive relations based on bulk samples can confidently be used to describe the behaviour of the surface material.

Table 1
Compositions of studied alloys in weight percent (wt.-%).

Alloy	Mg	Si	Fe	Cr	Cu	Mn	Al
6061	0.9	0.7	0.5	0.2	0.2	0.1	Base
6016	0.4	1.1	0.2	–	0.1	–	Base

2. Materials & methods

In this section, the approaches used in the current investigation are detailed in terms of materials used, experiments performed, and numerical model of the indentation.

2.1. Materials

Two commonly hot rolled aluminium alloys are studied in this work: a 6061 and a 6016. The 6xxx series contain Mg and Si as the main alloying elements [55]. The compositions of the studied alloys are shown in Table 1.

In hot rolling of aluminium, *thermo-viscoplasticity* of the material, i.e., the interdependence between stress, strain, time, temperature, and plasticity, is a major aspect. Different phenomenological constitutive models for alloys under hot working conditions are available in the literature [56]. In essence, macroscopic thermo-mechanical experimental results are fitted to a mathematical function representing the material model. The flow stress data for the 6061 aluminium alloy, or simply AA6061, can be found in a previous work [56], while the AA6016 data are presented in Section 2.3. Apart from the fact that the AA6016 samples were cut out of the end of a 450 mm thick ingot, its flow stress data were obtained and experimented in the same way as the 6061 alloy, except for a smaller strain range. This means that the flow curves of both alloys originated from compression tests of bulk samples initially cut out of the respective alloy ingots in as-cast conditions according to the actual rolling process. The hot compression tests were carried out using cylindrical samples in a Gleeble HDS-V40 machine, where a controlled nitrogen atmosphere is used and the desired forming temperature of the temperature is kept constant for 30 min before deformation starts at the desired strain rate. Mo_2S-Graphite suspension is used between samples and anvils to minimise friction. After the load–displacement raw data is processed to correct for friction, temperature and heat generation, results in terms of true plastic (flow) stress × true plastic strain data are generated, i.e., flow curves. By definition, the flow curve starts at the end of the elastic region, but strain offset approaches used in tensile tests are normally not applicable in hot forming tests. Thus, the initial yield stress is defined by looking for a clear transition from elastic to plastic region, while comparing with other flow curves. The block used to cut out specimens and samples for the hardness tests was obtained from ingots of identical composition and rolled with a few passes.

2.2. Experiments

Vickers hardness was employed throughout this work. The indenter comprises of a square-based pyramid whose opposite sides meet at

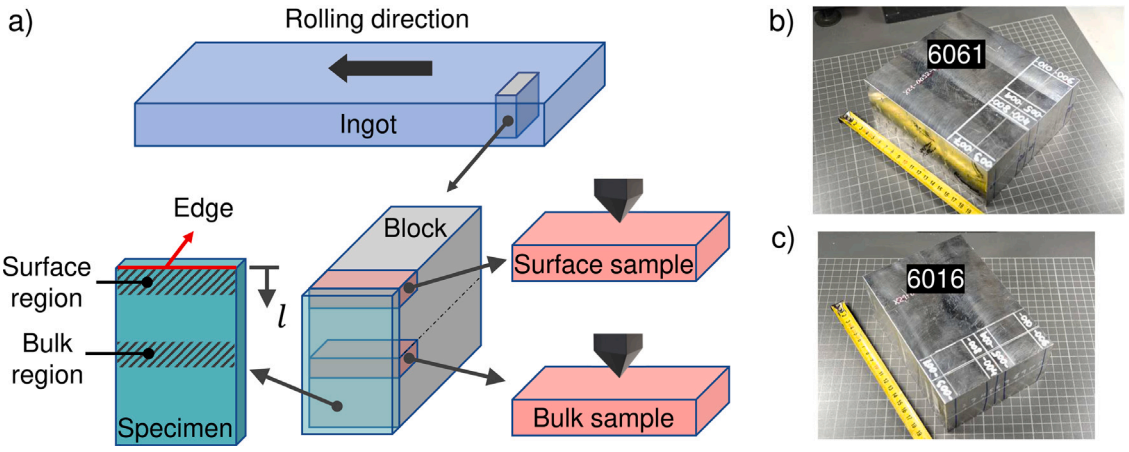

Fig. 1. (a) Positions of block, specimen, surface and bulk regions, and samples relative to ingot and rolling direction. Illustration of the indenter shows surface where high temperature indentations were performed on samples. Photos of actual blocks from which specimens and samples were cut: (b) AA6061 and (c) AA6016.

the apex with an angle between faces of 136°. Such indenter allows a wide range of strain and strain rate to be achieved within a single indentation, which is advantageous for evaluating viscoplasticity of the material. It is well-known that the Vickers indenter is designed to give geometrically similar indentations [57], such that the hardness should be independent of indentation size. The particular stress and strain fields depend on the material and conditions involved [58]; in case of the thermo-viscoplastic aluminium alloys studied in this work, whether the interplay between strain hardening, strain rate hardening, and softening with increasing temperature allow for similarities between each case is discussed in Section 3.4. Additionally, the goal is to evaluate the material properties as a whole in order to compare it with the material model, and not of its individual components such as precipitates and matrix, for which nanoindentation could be a more appropriate method.

The Vickers hardness HV has units of $\mathrm{kgf/mm^2}$ and is calculated using the actual surface area of the impression [57]:

$$\mathrm{HV} = \frac{L}{d^2/\left(2\sin\frac{136°}{2}\right)} = 1.8544\frac{L}{d^2} \tag{2}$$

where L is the load in kgf used in the experiment and added in the notation: in case of a 10 kg load, the notation used will be HV10. The variable d is the average of both diagonals of the indentation projected area.

The nomenclature used in this work is displayed in Fig. 1, along with indicated positions and a reference coordinate l, which is the distance from the edge of the specimen; the definition of the start and end of a *surface* region is to be determined from the experiments, according to the identification of any difference in the properties. Specimens were used in the RT tests, while surface and bulk samples were used in the HT tests.

An optical light microscope Carl Zeiss Axio Imager M2 m with a circular differential interference contrast filter was used to study the microstructure of the surface and bulk region in detail. RT hardness tests were performed at different loads and length scales on specimens, in attempts to determine any change in the properties between surface and bulk regions. Future Tec FV-700 and FM-700 were employed to perform RT Vickers macro- and micro-hardness tests, respectively. The HT Vickers hardness tests were performed on surface and bulk samples cut out of the block, as indicated in Fig. 1, in a test rig developed at AC2T research GmbH [59]. The indenter applies the set load through a system of springs in a defined period of time according to the Vickers standard. A load of 10 kg allows characteristics of different phases (if present) of the alloy to be averaged in the indentation [60], and therefore was used in the HT tests. Temperature is controlled in the samples through thermocouples and the indenter is a highly insulating material; thus, the sample temperature varies only a couple of °C during indentation, which is assumed not to affect the results. Three indents at each temperature were done to ensure repeatability and the diagonals of each indent were measured after cooling down using optical microscopy. The effect of cooling in the measurements is not considered significant: the coefficient of thermal expansion of the aluminium is approximately $23\times10^{-6}\,\mathrm{K^{-1}}$, which means that for a temperature difference of 400 K, the relative change in linear dimensions is about 1%, which can be considered within the range of measurement uncertainties. Low vacuum conditions (5 mbar) prevent oxidation during the tests. For the current work, the temperatures investigated were: 22 °C (room temperature), and from 50 °C to 450 °C in steps of 50 °C.

2.3. Finite element model

The commercial software COMSOL Multiphysics® v. 5.2a, which is based on the Finite Element Method, was used to perform time-dependent simulations of HT Vickers indentations. There are two domains in the 3D space model: the indenter on top and the aluminium sample below. The size of the sample was taken as that of the actual samples of the tests, which was approximately 68×20×10 mm in length, width and height (corresponding to y, x, z directions in the figure, respectively). However, using symmetry conditions, only a quarter of the whole geometry needs to be explicitly modelled, as shown in Fig. 2-(*a*). The software's *solid mechanics* module is employed and a penalty formulation is used for the frictionless contact between indenter and sample. Even though friction inevitably exists between the indenter and sample, a frictionless contact was set to simplify the model; in Section 4 it is shown that friction does not have significant effects in the hardness calculation and so, that a frictionless contact is acceptable. The software's tetrahedral meshing algorithm is used and the element type was set as second-order Lagrange elements. Structurally, the sample bottom boundary is fixed and the indenter is modelled as a rigid body with constrained rotation around all axis and constrained displacement in x, y-directions. A force L as a function of time is applied in the indenter domain in the negative z-direction, i.e., towards the sample. The function of the prescribed force over time was reproduced as that occurring in the HT hardness tests, shown in Fig. 2-(*b*).

When not only work hardening, but also strain rate and temperature effects are important, the flow stress of the material can be described using phenomenological constitutive equations in the form $\sigma_f = f(\varepsilon, \dot{\varepsilon}, T)$, i.e., the true flow stress σ as a function of strain ε, strain rate $\dot{\varepsilon}$, and temperature T. In these circumstances, the hardness would depend on the *indentation speed* and the *dwell time* [61,62]. Thus, a correct description of the force with respect to time is essential for

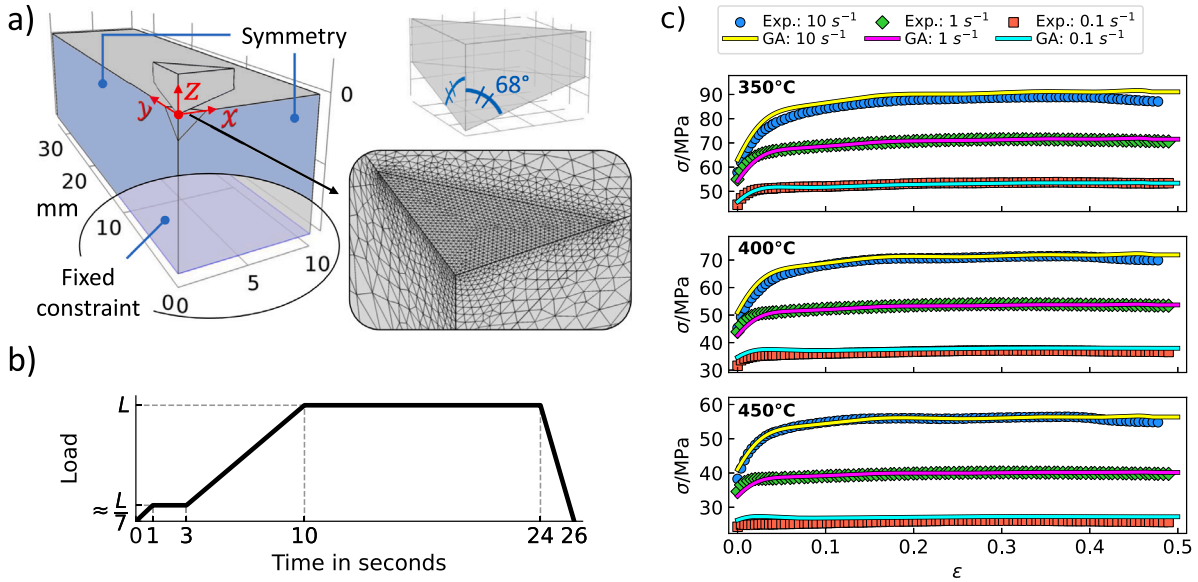

Fig. 2. (a) FE model with indicated boundary conditions, Vickers indenter geometry and FE mesh of sample contact region are detailed; b) Load applied on indenter domain in $-z$ direction; c) Predicted (GA) and experimental (Exp.) true flow stress of AA6016 as a function of true plastic strain, at different strain rates (0.1, 1 and 10 s^{-1}) and temperatures (350, 400 and 450 °C) – selected data are displayed for experimental values.

modelling the indentation of the experiment. The typical force vs time observed in the HT hardness tests is shown in Fig. 2-b). The start corresponds to a pre-loading step, whereas the end corresponds to the unloading of the indenter. A smoothing using piece-wise polynomials is applied at the transition points, particularly around 3 s and 10 s, which improves convergence in the simulation and, in fact, further approximates the profile to the actual one observed in the experiment. A spring foundation condition is applied to the indenter domain to prevent rigid body motion at the start of the simulation, basically functioning as a temporary weak spring, whose stiffness decays to zero after 3 s, when contact is already established.

The equation of the material model for the aluminium domain allows to capture the speed and dwell effects:

$$\dot{\varepsilon} e^{Q/RT} = A\left(\sinh\left(\alpha\sigma_f\right)\right)^{n'} \tag{3}$$

where σ_f is the flow stress, $\dot{\varepsilon}$ is equivalent plastic strain rate, T is temperature, $R = 8.3145\,\mathrm{J/mol/K}$ is the universal gas constant and Q, which is the deformation activation energy, along with the other material "constants" A, α and n', are represented as high-order polynomial functions of the equivalent plastic strain ε (details in Appendix). The left term of Eq. (3) is the Zener–Hollomon parameter [63], while the right term was suggested by Garofalo [64] and brought together by Sellars and McTegart [65]. This phenomenological constitutive model was showed by [64] to properly describe the material behaviour at low and high stress levels under creep conditions and is often referred to as "Arrhenius type equation" or "sine-hyperbolic". Here, it is referred to as Garofalo–Arrhenius, or simply GA model.

The experimental data and GA material model used for the AA6061 can be found in [56], as well as the steps to build such a model from flow curves. For the AA6016, experimental data and model prediction are shown in Fig. 2-c); the Pearson coefficient and average absolute relative error between flow stress prediction and experiment were 99.84% and 1.75%, respectively. Numerically, the model considers strain rate effects for $\dot{\varepsilon} \geq 0.001\,\mathrm{s}^{-1}$. For strain extrapolations beyond experimental data, i.e., $\varepsilon > 1$ for the AA6061 and $\varepsilon > 0.48$ for the AA6016, the flow stress is calculated by setting ε fixed at 1 and 0.48, respectively. Extrapolation of the flow stress prediction assuming constant values may be inaccurate if the prediction is made at much larger values of strain rate, at which the material behaviour can vary significantly [66]. Nonetheless, it is shown in the results that levels of strain rate are within the same order of magnitude as the experimental data. With regards to strain, a constant extrapolation is a reasonable approach, as shown by experiments at large strains [67–69]. For the sake of completeness, the aluminium domain of the FE model also contains elastic properties, set as standard aluminium values of 70 GPa for Young's modulus and 0.33 for Poisson's ratio. These are, however, irrelevant, since flow stress is reached practically as soon as the contact is established. Elastic recovery of the sample during unloading was also verified to be negligible. Finally, plasticity was based on multiplicative decomposition of the deformation gradient, by selecting *large plastic deformation* in the software.

3. Results

In this section, results of the experiments are presented and described while comparing the surface and bulk for both alloys. Optical microscopy is presented first, followed by room temperature hardness tests. Next, the HT hardness tests are presented and lastly, a simulated indentation is analysed.

3.1. Optical microscopy

The images obtained through optical microscopy of the bulk and surface regions of each alloy are shown in Fig. 3. The differential interference contrast technique was chosen to highlight precipitations and grain boundaries of the alloys; it shows the aluminium matrix in blue and the precipitates of the alloy as the coloured spots. It should be noted that this microscopy technique makes the precipitates seem larger than they actually are in the low magnification images.

Despite of this size effect, the distinction of the two alloys is evident with respect to size of grains and precipitates, with the AA6061 being noticeably larger and coarser. Contrasts in the matrix areas correspond to grain boundaries (GB), where hard phases precipitated.

Fig. 3 shows the grains are noticeably elongated in the direction of rolling for both alloys. The width of the grains differs between surface and bulk, indicating a stronger deformation at the surface region, and possibly resulting in different mechanical properties between bulk and surface.

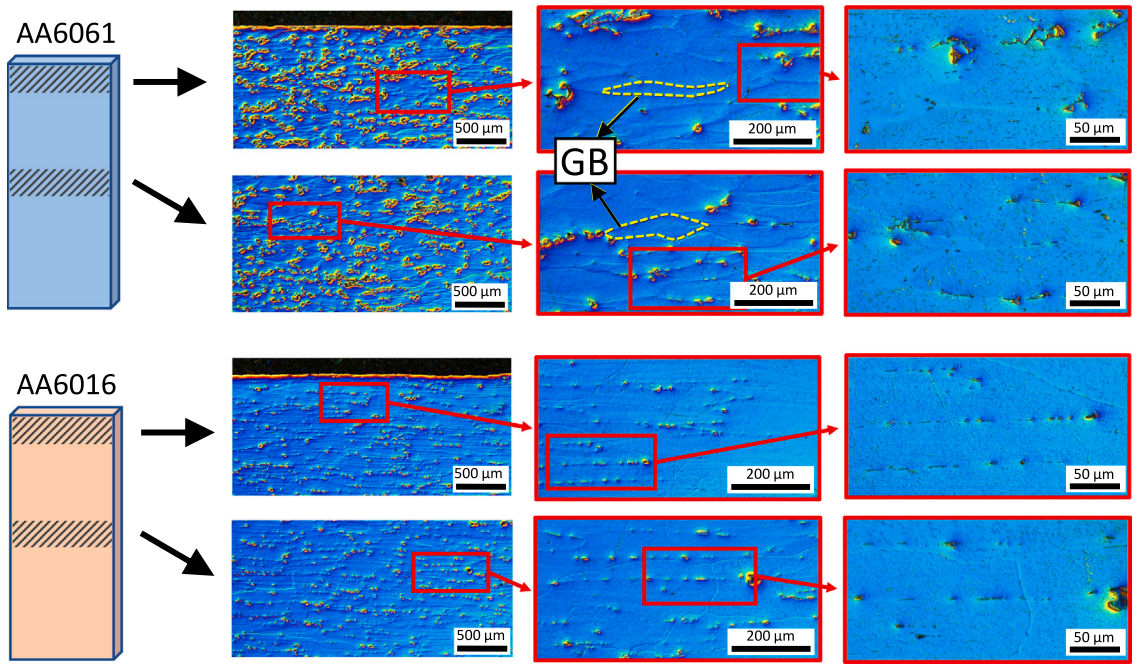

Fig. 3. Optical microscopy images using a circular differential interference contrast filter. Images obtained at indicated regions of the alloys' specimen corresponding to the surface and the bulk. Coloured spots are precipitates of the alloys; dashed contour lines details GB (grain boundary).

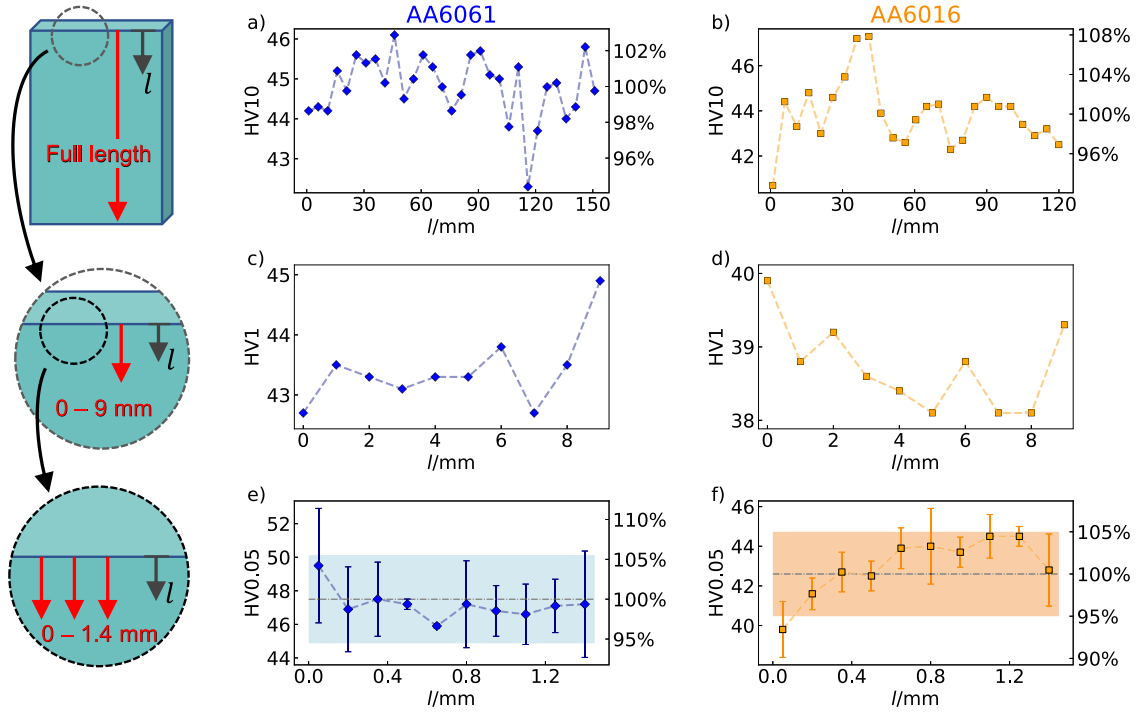

Fig. 4. Room temperature Vickers hardness results for AA6061 (blue diamond markers) and AA6016 (orange square markers). Images (a) and (b) correspond to load of 98.1 N (HV10) and was performed across full length of specimens; right-side percentage deviation is with regards to the average: 44.8 HV10 for AA6061 and 43.9 HV10 for AA6016. Images (c) and (d) correspond to load of 9.81 N (HV1) and was performed up to 9 mm from edge. Images (e) and (f) correspond to load of 0.49 N (HV0.05) and performed up to 1.4 mm from edge: markers are the average of 3 indents and error bars indicate ± a standard deviation. Black dash-dotted line and filled region represent bulk average ± a standard deviation, namely 47.5 ± 2.6 HV0.05 for AA6061 and 42.6 ± 2.1 HV0.05 for AA6016.

3.2. Room temperature hardness

Loads of 98.1 N (HV10), 9.81 N (HV1) and 0.49 N (HV0.05), the latter of which can be classified as micro-indentation [57], were used for the RT hardness tests. Hardness is obtained according to Eq. (2) by measuring the diagonals after the experiment is done. Attempts to identify any difference between surface and bulk regions are summarised in Fig. 4, as a function of the distance from the edge *l*. With HV10, the AA6061 has a fairly constant hardness value throughout the length of the specimen. More variation occurred with the AA6016, in which the first indentation (nearest to the edge) shows about 7% lower hardness relative to the average, which, however, was not observed

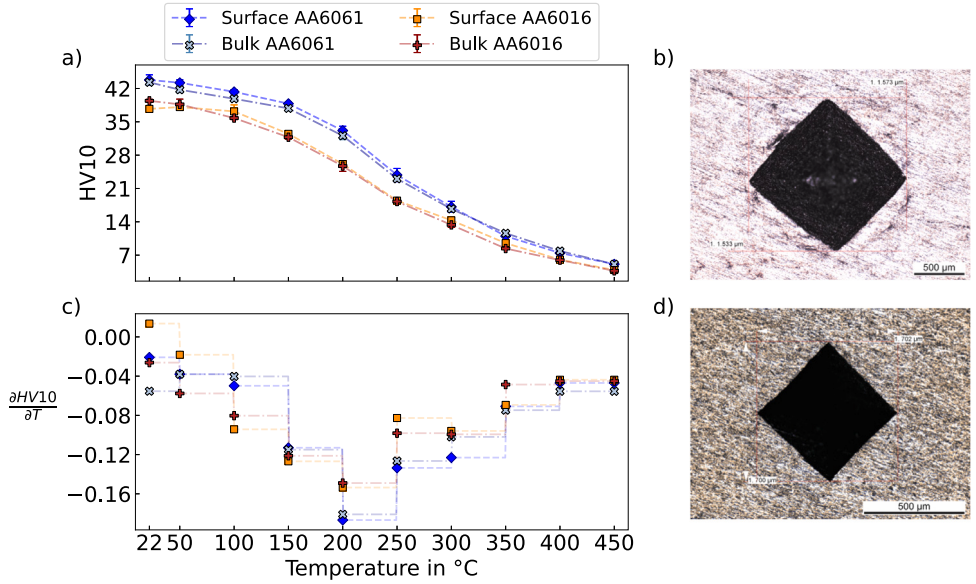

Fig. 5. (a) High temperature Vickers hardness using 10 kgf; values are average of 3 or more indentations and error bars indicate ± a standard deviation. (c) Corresponding hardness decrease rate with temperature. As examples, images of indentation marks are shown for (b) bulk of a AA6061 sample at 400 °C and for (d) surface of a AA6016 sample at 50 °C.

at the opposite position at $l \approx 120$ mm. Indentations at smaller length steps using HV1 show a clear difference between the two alloys, but no evident distinction between surface and bulk regions is observed; the lower hardness closer to the edge seen with HV10 for the AA6016 was not observed, which would suggest it is not a reflection of different properties.

An even smaller length scale was investigated in more detail using a load of 0.05 kgf. In this case, 3 indentations were performed at each position. 10 indentations were also performed in the bulk region to obtain an average and a standard deviation of the bulk hardness in order to compare with the surface region. The results are shown in images (e) and (f) of Fig. 4 as a function of l. The HV0.05 results shows that hardness in the bulk region can lie in a relatively wide range, which makes the values obtained in the surface region not statistically significant variations. Nonetheless, indentations closest to the edge, i.e., at approximately $l = 0.05$ mm showed largest difference with respect to bulk value in both alloys, with a nominal lower hardness for the AA6016 lying outside the expected value of the bulk. These results are further discussed in Section 4.1.

3.3. High temperature hardness

The results of the HT hardness tests are summarised in Fig. 5; samples of the surface and bulk were analysed for each alloy. It can be seen that the surface hardness of the AA6061 is slightly, but consistently, above the bulk value for temperatures between 50 °C and 250 °C. Considering the small uncertainty, this result could indicate a harder surface, albeit a small one. Apart from that, no other pronounced distinction is observed. Overall, the AA6061 starts at 43 HV10, reducing slightly until 150 °C, followed by a steep decline until the highest tested temperature, reaching 5 VH10 at 450 °C. The AA6016 reduces slightly from 38 HV10 until 100 °C, which is followed by a steep decline until 250 °C, and from that point onward, a lower rate is observed until about 4 HV10 at 450 °C. Both alloys have a similar softening curve, except the AA6061 is harder than the AA6016 by approximately 5 HV10 up to 250 °C; from this point onward, it softens slightly faster than the AA6016 such that the values approach one another.

The HT hardness tests evidence the non-linear decrease in hardness with increasing temperature. The rate at which hardness changes with respect to temperature can be visualised by taking the derivative of the experimental data, shown with an assumed constant rate for visualisation purposes in Fig. 5-b).

3.4. Finite element model

Initially, simulations were done for temperatures of 400 °C, and 450 °C for the AA6061, and 350 °C, 400 °C, and 450 °C for the AA6016. These temperatures are usual hot rolling temperatures for these alloys and lie within the range at which the respective material models were built, and so, within the range at which the flow stress can be reliably predicted. Firstly, the effects of temperature on the indentation are studied by analysing the plastic strain and strain rate fields of the solution. A FE mesh size convergence study was performed to ensure the results are minimally affected by its size; the indentation size and the average plastic in the indentation region were both used as metrics and the convergence criterion was that these parameters should not differ more than 0.5% between two mesh refinements for an acceptable FE mesh. The model of the AA6016 at 450 °C was chosen, since that is the case of largest deformation. Fig. 6-a) shows the mesh convergence results; the selected mesh contained approximately 2.72 million degrees of freedom and was used in all simulations.

The figure also shows the equivalent plastic strain field and maximum plastic strain for each temperature. Since the load applied in time is the same for all simulations, the softening of the aluminium at higher temperatures results in a bigger indentation mark than at lower temperatures. Consequently, the deformation of the sample at the end of the indentation increases with temperature, which is evidenced by the maximum equivalent plastic strain in Fig. 6-c). The same general strain pattern shown in image b) was observed throughout the indentation and temperatures, which is similar to the quasi-static pattern presented by [54], suggesting the strain hardening plays a major role in the overall hardening.

Similarly, the strain rate was observed to also generally increase, but its value changes significantly during the simulation because of the complex effects of constant and increasing load on the deformation of the material. Fig. 6-e) shows the maximum computed strain rate value, $\dot{\epsilon}_{max}$ for each temperature throughout time. The peak at the beginning corresponds to the instant of initial contact, which is inevitably computed as high strain rate due to the change between no-contact to contact. Low strain rates occur after 10 s, which corresponds to the constant load on the indenter (Fig. 2). The typical strain rate pattern during the indentation is displayed in image f), showing how the higher rates occur at the edge of the contact between indenter and sample.

The results show that higher temperatures do not necessarily lead to higher plastic strain rates throughout the entire indentation, but

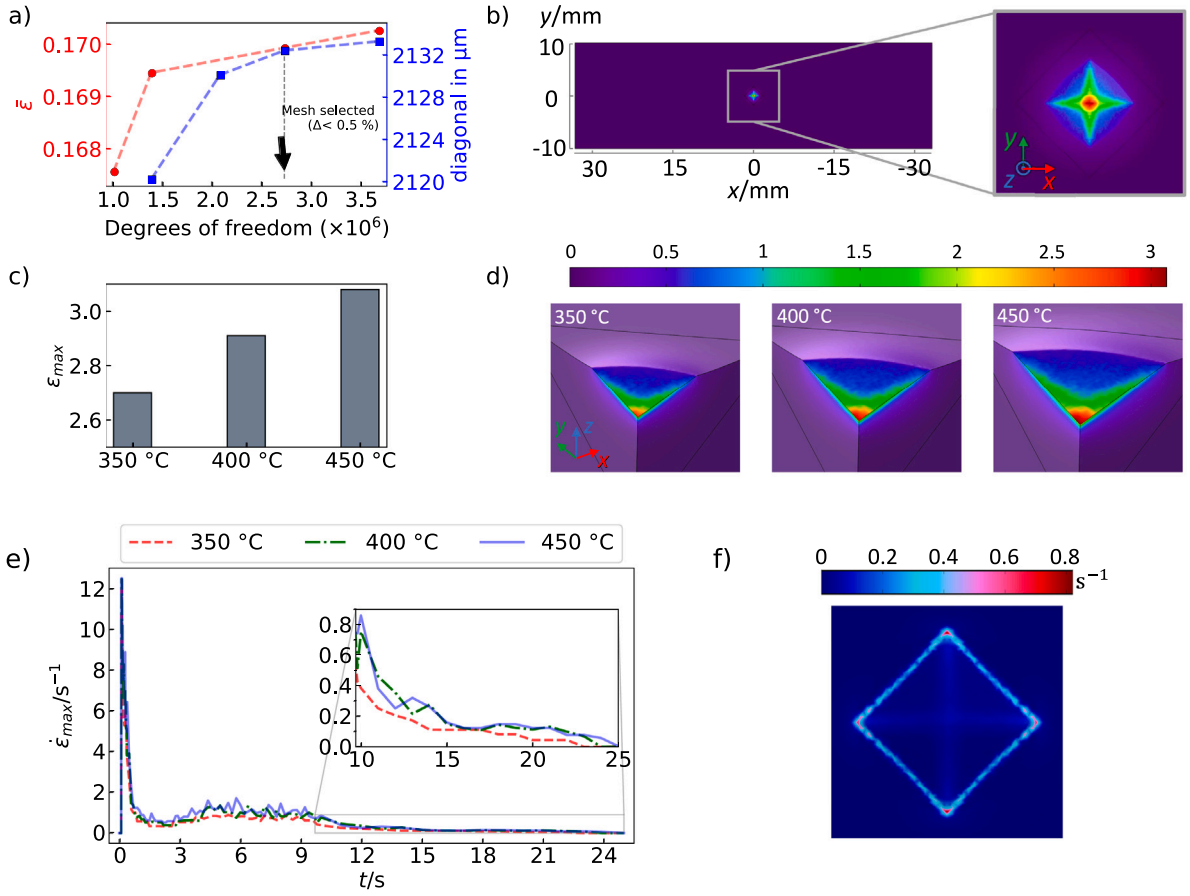

Fig. 6. Detailed results on simulations of indentations on AA6016. a) mesh convergence analysis considering average equivalent plastic strain $\bar{\varepsilon}$ in indentation region and diagonal of indentation (AA6016 at $T = 450\,°C$); selected mesh showed difference of quantities (Δ) below 0.5% in comparison to previous and subsequent meshes. b) mirrored solution on full aluminium domain and detail of typical plastic strain pattern. c) maximum equivalent plastic strain $\dot{\varepsilon}_{max}$ at indicated temperatures and corresponding d) equivalent plastic strain field at $T = 350\,°C$, (*b*) $T = 400\,°C$, and (*c*) $T = 450\,°C$. (e) Maximum equivalent plastic strain rate computed during indentation of AA6016 at different temperatures. Constant load region ($t > 10\,s$) and f) typical strain rate pattern ($t = 7\,s$ at $T = 450\,°C$) are shown in detail.

rather that its integral with respect to time increases, i.e., the total plastic strain. Although most of the deformation occurs during the increase of the load, the time interval corresponding to the constant load also causes significant deformation, evidencing the importance of correctly describing the applied force in time. Another important aspect highlighted by Fig. 6-e) refers to the importance of an accurate material model capable of capturing strain rate effects already at small values; it was verified that when using a material model that considers strain rate effects starting at $\dot{\varepsilon} \geq 0.1\,s^{-1}$ such as those presented in [39], the deformation during the constant load time interval is practically nonexistent, which resulted in different hardness values.

4. Discussion

In this section, the results presented in the previous section are discussed. Possible differences between surface and bulk are analysed, constraint factor maps relating the high temperature hardness and the material model are presented, and comparisons between experiment and simulations are looked in detail.

4.1. Hardness

The RT results presented in Figs. 3 and 4 indicate that, in general, there is no significant difference in room temperature hardness between bulk and surface of the alloys and at the length scales investigated. The difference in absolute values using different loads (HV10 vs HV0.05) can be attributed to either measurement deviations or indentation size effects; at smaller loads, the elastic part of the deformation has a higher fraction of contribution in the maximum deformation, i.e., the residual measured indent represents a smaller fraction of the total deformation (when the indenter is at maximum depth).

The micro-hardness results displayed in Fig. 4 showed the highest variation in the uppermost indentations, i.e., at the position of $l \approx 0.05\,mm$ for both alloys. The values suggest a tendency for a harder surface region for the AA6061, but a softer surface region for the AA6016. Even though the standard deviation would indicate that such differences are not statistically significant for the AA6061, the same tendency was observed in the HT hardness tests up to 250 °C (Fig. 5). Such difference can be attributed to some anisotropy of the material at the surface region due to slightly different grain structure, which was also observed in the optical microscopy (Fig. 3). Microhardness anisotropy was not investigated since the focus lies on comparing the indentations to the bulk-based material model, which is isotropic. The potential anisotropy seen in the hardness tests and microscopy may indeed lead to dissimilarities between simulation and experiment, but it is unlikely to be a strong source of errors given its small intensity. Anisotropy can result in different hardness depending on the orientation [70], but such investigations are more pertinent to single crystals and preferably done by means of the Knoop indenter [71].

The decrease rate of hardness with temperature in Fig. 4-b) shows that the fastest softening occurs between 200 °C and 250 °C, reaching the value of about $-0.18\,HV10/°C$ for the AA6061 and somewhat less for the AA6016. Considering that the melting temperature T_m of the alloys ranges between 580 to 650 °C [72], this corresponds to approximately 0.3 to 0.4 times T_m. It is well known that at such range, metals start to

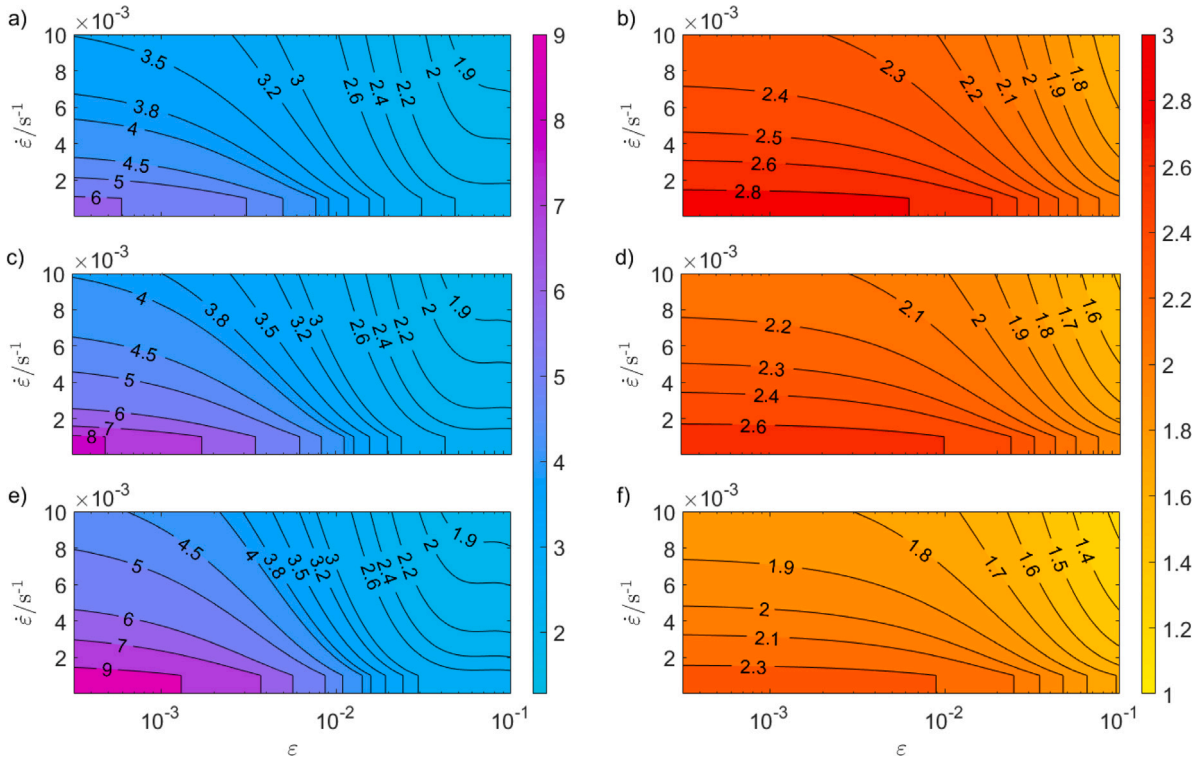

Fig. 7. Constraint factor map for alloys at selected ranges of strain (in log scale) and strain rate (in linear scale) such that relation (1) results in measured hardness: (a) AA6061 at 350 °C, (b) AA6016 at 350 °C, (c) AA6061 at 400 °C, (d) AA6016 at 400 °C, (e) AA6061 at 450 °C, and (f) AA6016 at 450 °C.

Table 2
Hardness ± standard deviation in MPa.

Alloy	350 °C	400 °C	450 °C
AA6061	111.39 ± 4.53	75.51 ± 3.05	49.98 ± 1.10
AA6016	87.80 ± 6.06	58.89 ± 1.55	37.14 ± 1.17

creep significantly; the phenomenon has also been observed for other metals in HT hardness experiments [35].

4.2. Constraint factor

In this subsection, the constraint factor in Eq. (1) is analysed by verifying the results of the HT hardness tests and the flow stress predicted by the material model of each alloy. Firstly, Table 2 shows selected measured hardness values in MPa.

In order to study if relation (1) can predict such values, the strain and strain rate at which the flow stress should be evaluated would need to be defined. The use of Tabor's representative strain is ill-suited because not only strain hardening is present. An analogous "representative strain rate" based on indenter velocity as discussed by [73,74] is likewise problematic because strain rate is not constant throughout the indentation. Instead, using the material model and the results from the hot hardness tests, we can build a "constraint factor map" to visualise c as a function of strain and strain rate at each temperature, using the nominal results of the hardness tests. This is shown in Fig. 7.

The visualisation reveals, firstly, that the value of $c = 2.8$ attributed to aluminium by Tabor is only correct in particular conditions of strain at strain rate, and in fact, only at 350 °C for the AA6016. In other words, hardness cannot be correctly predicted using $H = 2.8\sigma_f$ at 400 °C and 450 °C for the AA6016; in these cases and depending on chosen representative strain and strain rate, the maps shown in Fig. 7 can be used. An appropriate constraint factor for the AA6061 can be much higher than 2.8 and much lower for the AA6016. It is interesting

Table 3
Constraint factor by fixing strain and strain rate such that $c \times \sigma_f(\epsilon, \dot{\epsilon}, T)$ results in measured hardness of AA6061.

$(\epsilon, \dot{\epsilon})$	350 °C	400 °C	450 °C
(0,0)	6.34 ± 0.26	8.49 ± 0.34	10.72 ± 0.24
(0, 0.01)	3.44 ± 0.14	4.06 ± 0.16	4.76 ± 0.1
(0.01, 0.01)	2.62 ± 0.11	2.67 ± 0.11	2.77 ± 0.06
(0.08, 0.01)	1.83 ± 0.07	1.83 ± 0.07	1.85 ± 0.04

Table 4
Constraint factor by fixing strain and strain rate such that $c \times \sigma_f(\epsilon, \dot{\epsilon}, T)$ results in measured hardness of AA6016.

$(\epsilon, \dot{\epsilon})$	350 °C	400 °C	450 °C
(0,0)	2.92 ± 0.2	2.77 ± 0.07	2.44 ± 0.08
(0, 0.01)	2.33 ± 0.16	2.14 ± 0.06	1.84 ± 0.06
(0.01, 0.01)	2.19 ± 0.15	2.01 ± 0.05	1.72 ± 0.05
(0.08, 0.01)	1.67 ± 0.12	1.53 ± 0.04	1.31 ± 0.04

to note that the values for the constraint factor at fixed strain and strain rate changes differently for each alloy; for the AA6061, the values increase with temperature, while for the AA6016 the values decrease. The reason for this is can be attributed to the material model and the resulting hardness decrease rates for each alloy, which is overestimated for the AA6061, and underestimated for the AA6016 (shown in upcoming section). Tables 3 and 4 show constraint factor values of selected combinations of strain and strain rate for each alloy.

The results provide insights on how the constraint factor varies with temperature, and expose that it clearly depends on the values of strain and strain rate. These results show that care must be taken when using Eq. (1) to study hardness involving thermo-viscoplastic materials, requiring proper definition of the conditions being studied. Constraint factor maps such as that presented in Fig. 7 can now be used for such cases.

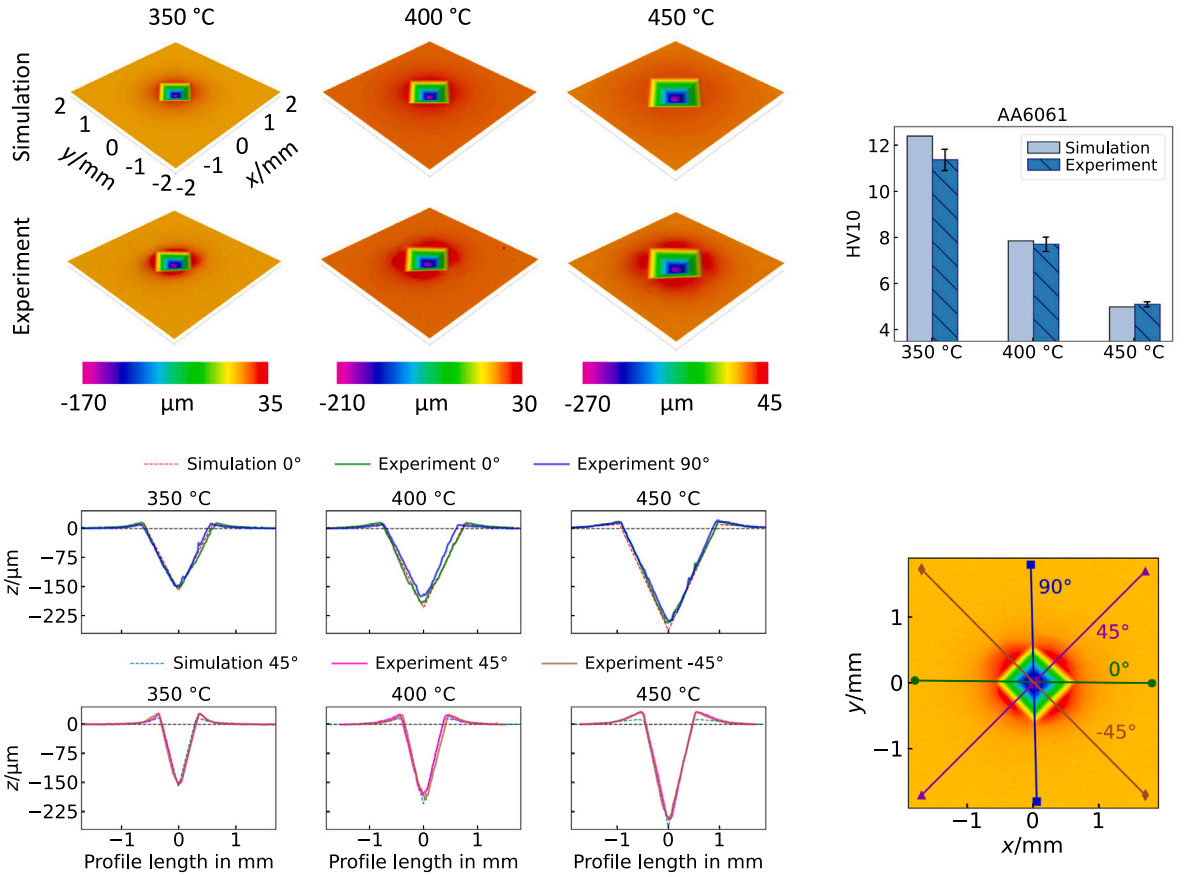

Fig. 8. Comparison of indentation mark geometry and cross-section profiles of simulations and experiments for AA6061 at indicated temperatures and directions. 3D surfaces shown are all 4×4 mm in size, as displayed for the simulation case at 350 °C. Hardness comparison is shown on the top right and directions of cross-sections on the bottom right.

4.3. Model vs experiment

In this subsection, the simulations are compared with the experimental results to verify the applicability of the bulk-based material model in describing deformation of the surface. For such purpose, the topography of indentation marks were measured using an Alicona InfiniteFocus® optical 3D measurement system.

Figs. 8 and 9 compare simulations and experiments for the alloys, showing the final 3D geometry of simulations and measured indentation marks, a comparison of hardness values between simulations and experiments and a comparison of cross-sections in the directions of the diagonals and 45° to it. The comparison of hardness is, in fact, a comparison of d_{FE} and d_{exp}, i.e., the diagonals of the indentation marks of simulation and experiment, respectively. The uncertainty of d_{exp} refers to the standard deviation of the measurements of the 3 indentation marks performed at each temperature and at each sample (bulk and surface). Similarly, d_{FE} is measured in both x and y directions, taken at the maximum pile-up height. Nonetheless, the diagonals of the indentation mark in the FE model were practically the same in both directions and so, a mean value of d_{FE} is calculated, and used as a single nominal value for simulated hardness.

It is important to restate that the material models implemented in the FE Vickers model are based on the compression flow curves of the alloys, and that no inverse modelling is performed in this work. Thus, the indentation results of the simulation and any temperature dependence can be independently compared to the HT hardness experiments. The topography measurement and the hardness comparison show overall a good agreement between model and experiment. The more noticeable overestimation for the AA6061 at 350 °C is not surprisingly, since this temperature corresponds to one outside the range at which the AA6061 material model was built — further discussion on predictions outside the experimental range is presented in Section 4.4. The hardness decrease rate with temperature is somewhat more pronounced in the FE model for the AA6061, leading to a slight overestimation of HV10 at 400 °C, but to a underestimation at 450 °C (with respect to the nominal experimental value). On the other hand, the AA6016 shows a slightly lower decrease rate with increasing temperature in comparison with the experiment (Fig. 9). As discussed previously, such behaviour explains the increasing or decreasing values seen for each of the alloys' constraint factor maps. Overall, the results in all cases are in excellent agreement with the experiment within the expected temperature range, which indicates that the material model based on flow curves of bulk samples and compression tests are indeed suitable to describe the material and its deformation at the surface level.

With regards to the cross-section profiles, the FE model is perfectly aligned and symmetrical in the 0° and 90° planes. The measurements, however, need to be manually aligned and so, these directions need to be visually set. Furthermore, since the indentation mark is not a perfect square indent nor is the indenter perfectly sharp, cross-sections rotated 90° are different from each other. For the AA6061, the predicted profile matches quite well with the experiment in the diagonal direction (0°), and the face direction (45°), except for the 450 °C case, where it is underestimated. For the AA6016, simulations are generally overestimating the profile changes. The experimental profiles of the two materials are generally very similar, but the simulated results are quite different. The reason for such difference is a consequence of the material model, since all other conditions in the model and experiment are the same. The reason for differences between simulations and experiment is evidently a consequence of the combined simplifications of the model: perfectly sharp and rigid indenter contacting the sample without friction nor heat transfer. The experiments also contained

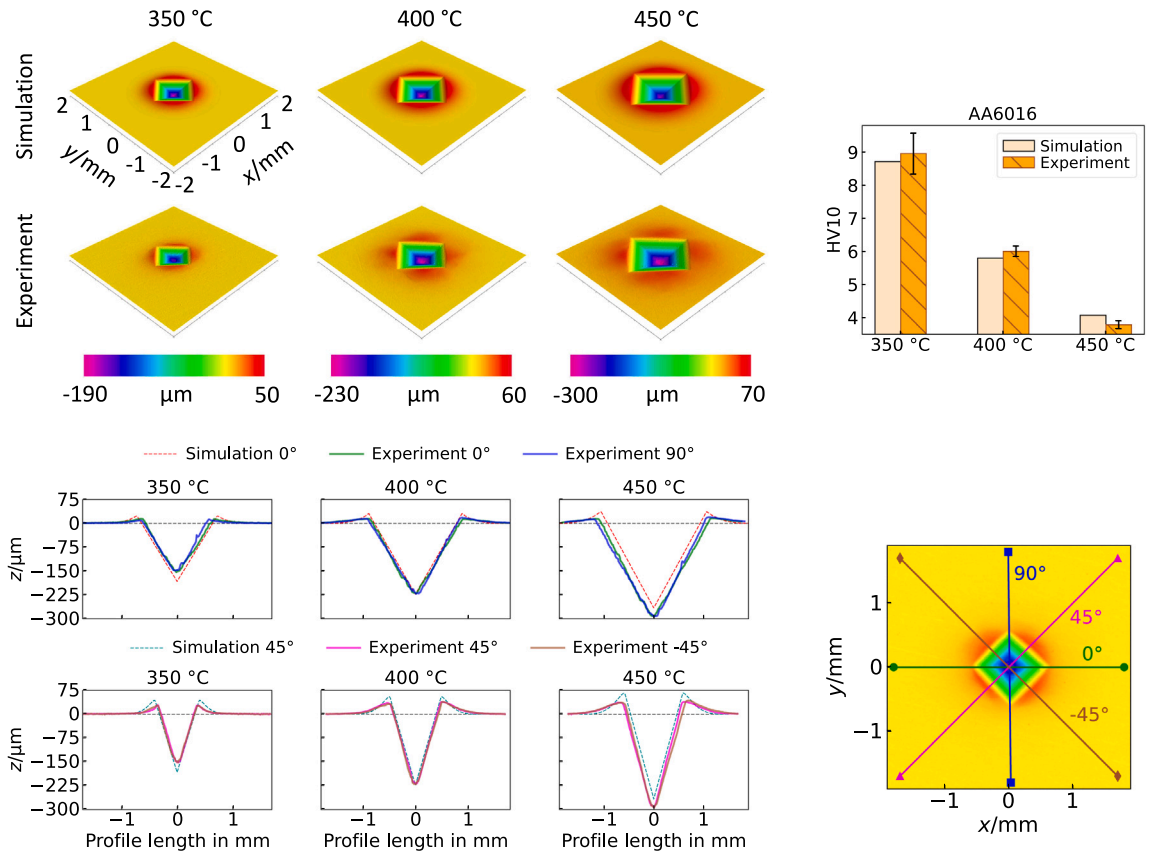

Fig. 9. Comparison of indentation mark geometry and cross-section profiles of simulations and experiments for AA6016 at indicated temperatures and directions. 3D surfaces shown are all 4×4 mm in size, as displayed for the simulation case at 350 °C. Hardness comparison is shown on the top right and directions of cross-sections on the bottom right.

"imperfections" such as asymmetry of the indentation marks, resulting in different profiles, which are difficult to achieve at HT since the setup shows different thermal expansions. The pile-up return to the original height, in general, is in good agreement with the measurements. Along the face cross-section profiles, which corresponds to approximately the middle of the indentation edge, pile-up is higher than that of the diagonal profile, both for simulations and experiments. Such effect has also been observed in high temperature hardness tests of other materials [75].

It was hypothesised that the presence of friction could play an important role in modifying the plastic flow of the surrounding material, and so, simulations were performed where a Coulomb friction model using different values of coefficient of friction (CoF) was analysed. The temperature of 450 °C was selected because of its larger plastic strain and so, better visualisation of differences between the models. The effects on hardness and on the pile-up can be seen in Fig. 10. The results show once again the complexity of the plastic flow around the indentation and the behaviour of the different materials; overall, it can be seen that it causes the material surrounding the indenter to be partly "dragged down", which reduces the pile-up. Nonetheless, the effects of friction on hardness can be considered negligible, which justifies the frictionless contact simplification for the model. The sudden drop in the AA6061, 0.2 CoF case is due to the fact that a sharp pile-up peak is no longer present: the methodology for selecting the diagonal in the simulations was the position of the profile with the highest z value; in the 0.2 case, this point has shifted further away form the indentation centre, rendering lower hardness. The effect of other simplifications such as heat transfer or rounded indenter tip were not investigated.

Despite the drawbacks regarding the pile-up, the results displayed in this section show, in general, a good agreement between model and experiment, which shows the effectiveness of the material model in the prediction of hardness and surface deformation.

4.4. Prediction at lower temperatures

In Fig. 8, it was showed that hardness at 350 °C had relatively good agreement with the experiment, even though the material model of the AA6061 was built based on temperatures ranging from 400 °C to 550 °C. Given the good predictions of the FE model, one may wonder if hardness at lower temperatures could also be predicted, i.e., at temperatures outside the experimental range on which the material models was based. To answer this question, simulations were computed at lower temperatures and compared with the experiments. The results are shown for both alloys in Fig. 11.

The simulations still provide quite a good prediction in the range of 200 °C to 300 °C. However, the model clearly overestimates the values at temperatures below 200 °C for both alloys. These results can be attributed to the distinct hardness decrease rate for each temperature range: since the material model was built based on the range of 350 °C to 450 °C, the hardness predicted by the model increases exponentially with decreasing temperature due to the Arrhenius term in the constitutive equation (equation (3)), which is indeed observed in Fig. 11. The actual material, however, has a complex temperature dependent deformation behaviour such that the hardness decrease rate dramatically changes at approximately 0.3 to 0.4 times T_m, as discussed previously in Section 4.1. Such information was not "available" to the material model fitted between 350 °C to 450 °C, hence, this change below 200 °C cannot be represented by the model.

The relative error between the hardness obtained by the experiment to that predicted by the FE model from 50 °C to 150 °C was calculated. In an attempt to improve the prediction of the FE model at this range, this relative error was interpreted as a correction factor K, i.e., $K = \mathrm{HV10}_{exp}/\mathrm{HV10}_{FE}$. This factor was used in additional simulations where the material model is multiplied by K at the respective temperature,

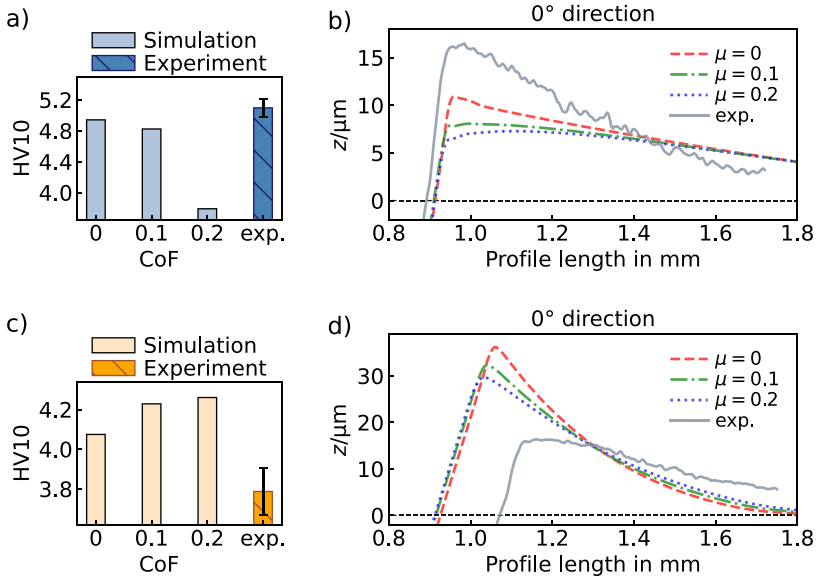

Fig. 10. Effects of including different values for the coefficient of friction (CoF) through a Coulomb friction model in the finite element model, using the case at 450 °C, and comparing with experimental results (exp.): effects on hardness for (a) AA6061 and (c) AA6016, and effects on pile-up region for (b) AA6061 and d) AA6016.

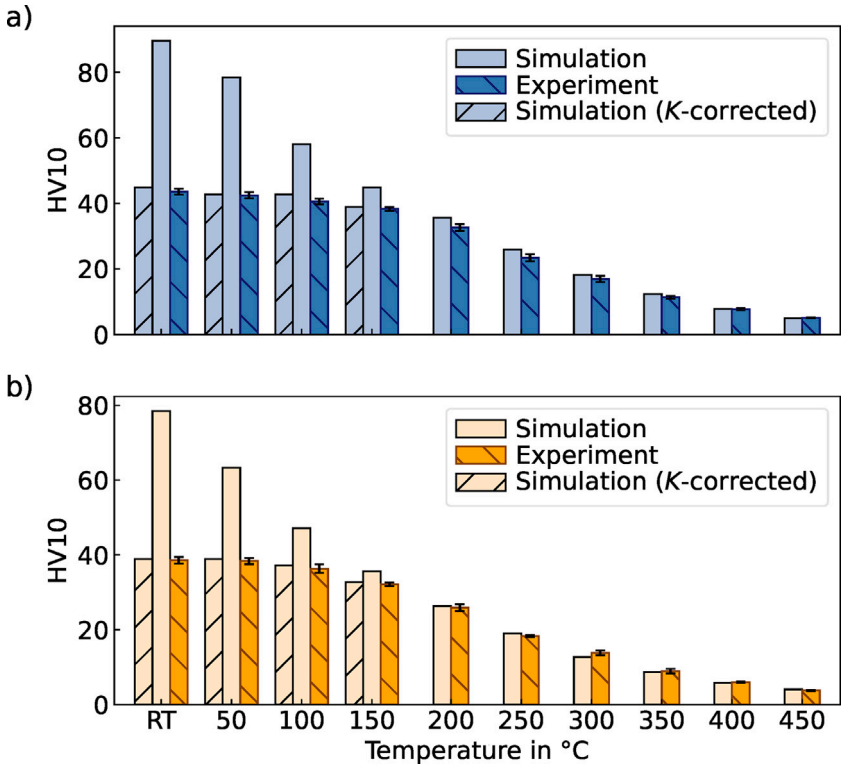

Fig. 11. Hardness comparison of simulations, experiments, and simulations using corrected material model for temperatures investigated: a) AA6061 and b) AA6016. RT: room temperature (≈ 22 °C).

which essentially artificially "softens" the material as a whole. Values used are shown in Table 5.

It should be highlighted, however, that the shape of the flow stress curve when using the material model in the extrapolated temperature

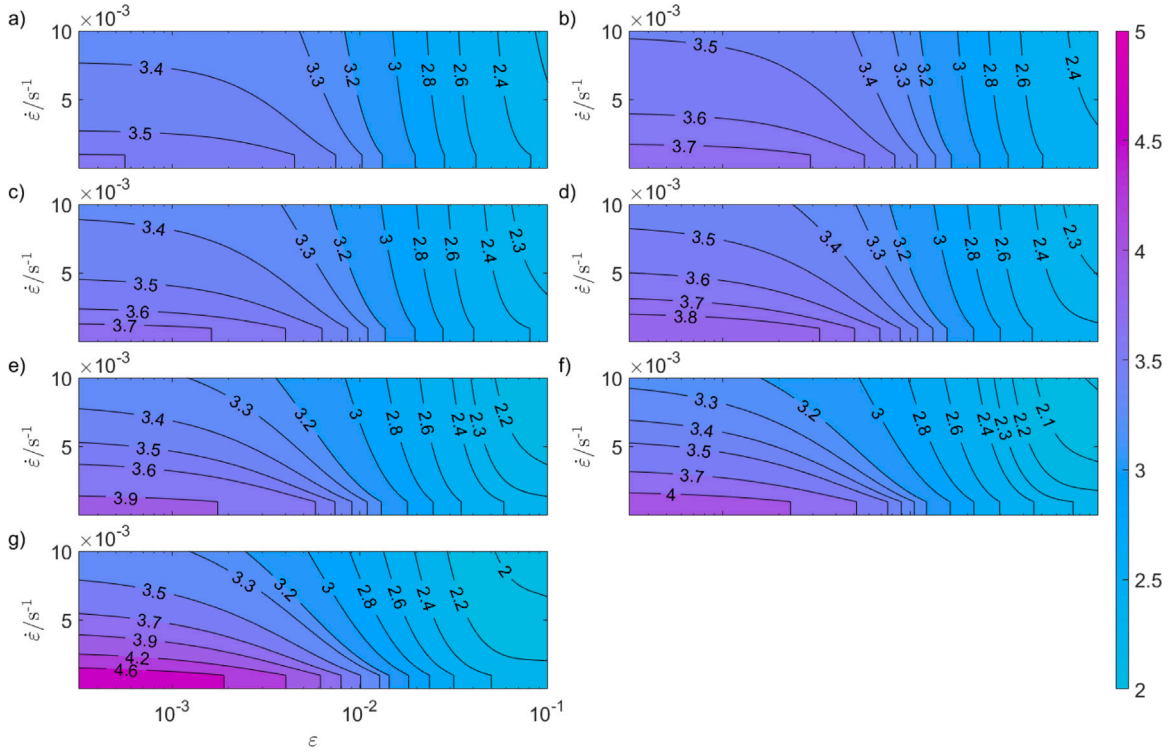

Fig. 12. Constraint factor map for AA6061 at selected ranges of strain (in log scale) and strain rate (in linear scale) such that relation (1) results in measured hardness: a) 22 °C, (b) 50 °C, (c) 100 °C, (d) 150 °C, (e) 200 °C, (f) 250 °C, and (g) 300 °C.

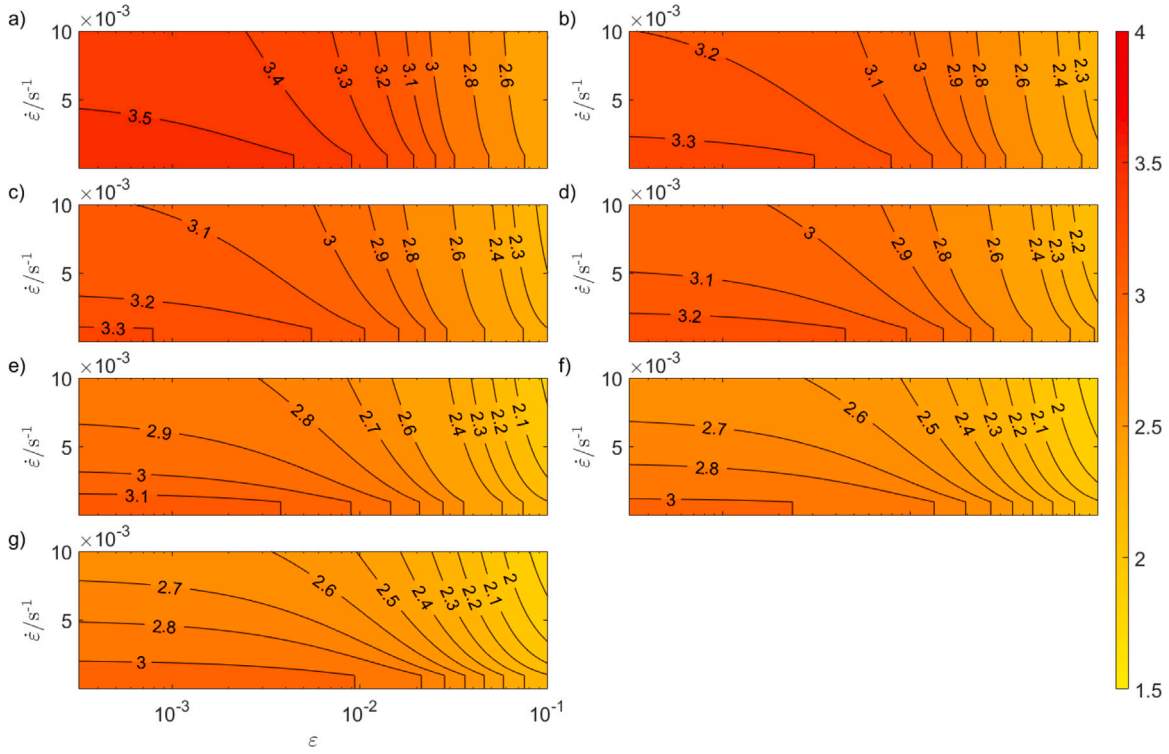

Fig. 13. Constraint factor map for AA6016 at selected ranges of strain (in log scale) and strain rate (in linear scale) such that relation (1) results in measured hardness: a) 22 °C, (b) 50 °C, (c) 100 °C, (d) 150 °C, (e) 200 °C, (f) 250 °C, and (g) 300 °C.

Table 5
Correction factor K used in simulations at lower temperatures.

Alloy	22 °C	50 °C	100 °C	150 °C
AA6061	0.49	0.54	0.7	0.85
AA6016	0.49	0.61	0.77	0.9

range, i.e., outside the range at which it was built, is unknown to be correct in terms of the material behaviour as a function of strain and strain rate. Nonetheless, the results suggest the flow stress correction using the "K-correction" works in terms of hardness prediction. When writing the correction factor as a function of temperature, its use in the flow stress equation could supposedly allow the FE model to predict hardness of the materials at low temperatures.

Constraint factor maps can also be build for the lower temperatures, using the correction factor in the material model. This is shown in Figs. 12 and 13 for the AA6061 and AA6016, respectively. As seen with the higher temperatures, the constraint factor can vary considerably from the usual range of 2.6 to 3 for both alloys.

The topography of the indentations at lower temperatures have also been measured and comparisons of the cross-section profiles are shown in Appendix B. In general, the same trends discussed in Section 4.3 were observed, namely, the predictions of the AA6061 in excellent agreement with the measurement, and the pile-up heights are overestimated by the model for the AA6016.

5. Conclusions

This work systematically studied how the bulk flow stress and the surface hardness of two aluminium alloys manufactured by hot rolling, i.e., the AA6061 and AA6016, relate to each other in metal forming conditions. Firstly, specimens of both alloys were analysed using a technique of optical microscopy and room temperature Vickers hardness. Results using different loads and at different length scales across the length of specimens are shown in order to identify differences in the material properties. No statistically significant difference was identified between bulk and surface for neither of the alloys, although the AA6061 presented a tendency for harder surface than its bulk.

Such tendency was also observed in high temperature hardness tests, where a slightly harder surface was present up to 250 °C for the AA6061, but overall no significant difference between bulk and surface was observed for neither alloy in the temperature range from room temperature to 450 °C. The non-linear evolution of hardness with temperature was quantified for the alloys, with the AA6061 being consistently harder than the AA6016.

The results from the high temperature hardness experiments were subsequently compared with the thermo-viscoplastic flow stress of each alloy, where the relation (1) can be evaluated. Constraint factor maps relating flow stress to hardness are presented which serve as ready-to-use charts for the selection of appropriate constraint factors, which are now shown to be dependent on temperature, strain and strain rate.

The numerical model is subsequently discussed and it is shown that the bulk-based material model accurately predicted hardness for both alloys at different temperatures. The general deformed geometry of the indentation marks were also reasonably predicted, except for a mismatch in pile-up height. Predictions at lower temperatures could be performed with the use of a correction factor, which subsequently also allowed the creation of constraint factor maps at lower temperatures for the alloys.

Conclusively, the elaboration of constraint factor maps performed in this work provide support to questions which have often been overlooked in the metal forming literature, namely, how hardness relate to the flow stress in temperature and time-dependent material conditions. Overall, the material model based on the bulk can be used to predict deformation at the surface level and so, can be employed for further studies in metal forming.

CRediT authorship contribution statement

André Rudnytskyj: Conceptualization, Methodology, Software, Validation, Formal analysis, Investigation, Data curation, Visualization, Writing – original draft, Writing – review & editing. **Markus Varga:** Methodology, Formal analysis, Investigation, Data curation, Writing – review & editing. **Stefan Krenn:** Supervision, Writing – review & editing. **Georg Vorlaufer:** Supervision. **Josef Leimhofer:** Resources, Writing – review & editing. **Martin Jech:** Project administration, Funding acquisition. **Carsten Gachot:** Supervision, Writing – review & editing.

Declaration of competing interest

The authors declare that they have no known competing financial interests or personal relationships that could have appeared to influence the work reported in this paper.

Data availability

The raw/processed data required to reproduce these findings cannot be shared at this time as the data also forms part of an ongoing study.

Acknowledgements

This work was supported by the Austrian COMET-Program (K2 Project InTribology, no. 872176) and carried out at the "Excellence Centre of Tribology" (AC2T research GmbH). The authors acknowledge TU Wien Bibliothek for financial support through its Open Access Funding Programme. Part of the data and images in this work were processed and created by means of free and open-source basis software [76–78].

Appendix A. Material model

The GA constitutive model used in this work relates a hyperbolic sine and the Zener–Hollomon parameter, along with strain dependence [79]. The material constants α, n', Q and A are expressed as polynomial functions of the equivalent plastic strain ε as:

$$\begin{aligned} \alpha(\varepsilon) &= C_0 + C_1\varepsilon + C_2\varepsilon^2 + \cdots + C_p\varepsilon^p \\ n'(\varepsilon) &= D_0 + D_1\varepsilon + D_2\varepsilon^2 + \cdots + D_p\varepsilon^p \\ Q(\varepsilon) &= E_0 + E_1\varepsilon + E_2\varepsilon^2 + \cdots + E_p\varepsilon^p \\ \ln\left[A(\varepsilon)/\mathrm{s}^{-1}\right] &= F_0 + F_1\varepsilon + F_2\varepsilon^2 + \cdots + F_p\varepsilon^p \end{aligned} \tag{A.1}$$

where C_i, D_i, E_i, and F_i with i from 1 to the degree of the approximation p are the regression coefficients and the term with $i = 0$ is the dependent variable intercept. For the AA6016, $p = 8$ was used for all constants and the values are shown in Table A.1. The values used for the AA6061 can be found in [56].

Appendix B. Indentation profiles at lower temperatures

See Figs. B.1 and B.2.

Table A.1
Polynomial coefficients for material constants of the GA model for the AA6016.

$\alpha(\varepsilon)$ /MPa^{-1}	$n'(\varepsilon)$	$Q(\varepsilon)$ / (kJ mol^{-1})	ln $[A_{GA}(\varepsilon)/\mathrm{s}^{-1}]$
$C_0 = 3.461649130 \times 10^{-2}$	$D_0 = 7.259729881$	$E_0 = 2.201285692 \times 10^{2}$	$F_0 = 3.400930110 \times 10^{1}$
$C_1 = -2.313705278 \times 10^{-1}$	$D_1 = -1.152346077 \times 10^{2}$	$E_1 = -2.314212137 \times 10^{3}$	$F_1 = -3.526878194 \times 10^{2}$
$C_2 = 1.587715962$	$D_2 = 2.496149313 \times 10^{3}$	$E_2 = 4.033439031 \times 10^{4}$	$F_2 = 6.918567136 \times 10^{3}$
$C_3 = 5.472363342 \times 10^{-1}$	$D_3 = -2.843677457 \times 10^{4}$	$E_3 = -4.142162809 \times 10^{5}$	$F_3 = -7.650805602 \times 10^{4}$
$C_4 = -7.216626499 \times 10^{1}$	$D_4 = 1.842947463 \times 10^{5}$	$E_4 = 2.570440481 \times 10^{6}$	$F_4 = 4.964410648 \times 10^{4}$
$C_5 = 4.378192869 \times 10^{2}$	$D_5 = -6.994873617 \times 10^{5}$	$E_5 = -9.567953216 \times 10^{6}$	$F_5 = -1.899652801 \times 10^{6}$
$C_6 = -1.201616018 \times 10^{3}$	$D_6 = 1.535262041 \times 10^{6}$	$E_6 = 2.075023864 \times 10^{7}$	$F_6 = 4.195565438 \times 10^{6}$
$C_7 = 1.606078004 \times 10^{3}$	$D_7 = -1.802034516 \times 10^{6}$	$E_7 = -2.409319041 \times 10^{7}$	$F_7 = -4.934454344 \times 10^{6}$
$C_8 = -8.461960825 \times 10^{2}$	$D_8 = 8.748063102 \times 10^{5}$	$E_8 = 1.155855647 \times 10^{7}$	$F_8 = 2.389914740 \times 10^{6}$

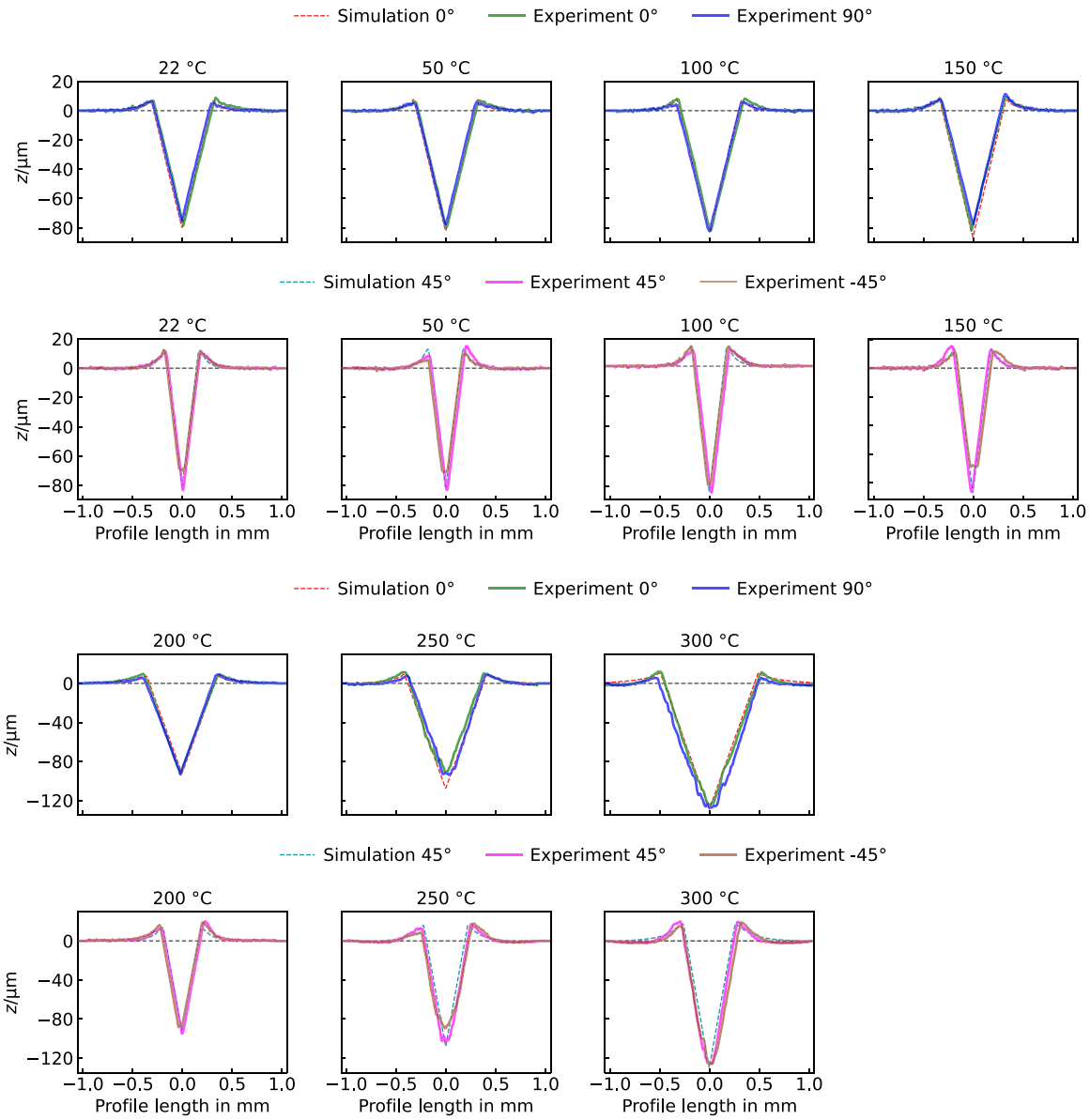

Fig. B.1. Comparison of cross-section profiles of simulations and experiments for AA6061 at indicated temperatures and directions according to Section 4.3.

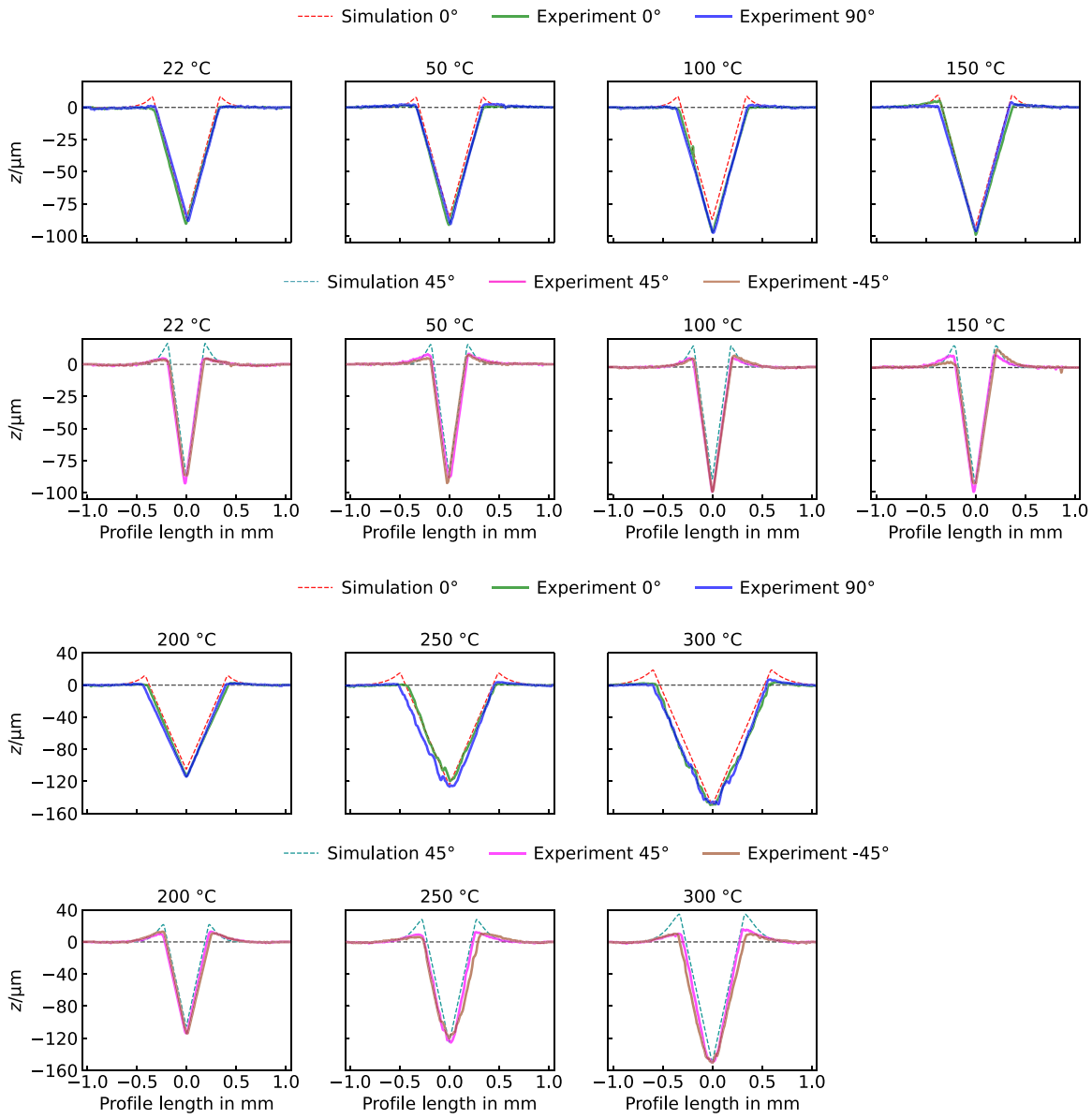

Fig. B.2. Comparison of cross-section profiles of simulations and experiments for AA6016 at indicated temperatures and directions according to Section 4.3.

References

[1] Hutchings IM. The contributions of David Tabor to the science of indentation hardness. J Mater Res 2009;24(3):581–9. http://dx.doi.org/10.1557/jmr.2009.0085.

[2] Tabor D. The hardness of metals. Oxford University Press; 1951.

[3] Tabor D. Indentation hardness: Fifty years on a personal view. Phil Mag A 1996;74(5):1207–12. http://dx.doi.org/10.1080/01418619608239720.

[4] Francis HA. Phenomenological analysis of plastic spherical indentation. J Eng Mater Technol 1976;98(3):272–81. http://dx.doi.org/10.1115/1.3443378.

[5] Cáceres C, Griffiths J, Pakdel A, Davidson C. Microhardness mapping and the hardness-yield strength relationship in high-pressure diecast magnesium alloy AZ91. Mater Sci Eng A 2005;402(1–2):258–68. http://dx.doi.org/10.1016/j.msea.2005.04.042.

[6] Khodabakhshi F, Haghshenas M, Eskandari H, Koohbor B. Hardness-strength relationships in fine and ultra-fine grained metals processed through constrained groove pressing. Mater Sci Eng A 2015;636:331–9. http://dx.doi.org/10.1016/j.msea.2015.03.122.

[7] Tiryakioğlu M. On the relationship between vickers hardness and yield stress in Al–Zn–Mg–Cu Alloys. Mater Sci Eng A 2015;633:17–9. http://dx.doi.org/10.1016/j.msea.2015.02.073.

[8] Sundararajan G, Tirupataiah Y. The hardness-flow stress correlation in metallic materials. Bull Mater Sci 1994;17(6):747–70. http://dx.doi.org/10.1007/bf02757555.

[9] Pavlina E, Tyne CV. Correlation of yield strength and tensile strength with hardness for steels. J Mater Eng Perform 2008;17(6):888–93. http://dx.doi.org/10.1007/s11665-008-9225-5.

[10] Asgharzadeh A, Tiji SAN, Esmaeilpour R, Park T, Pourboghrat F. Determination of hardness-strength and -flow behavior relationships in bulged aluminum alloys and verification by FE analysis on Rockwell hardness test. Int J Adv Manuf Technol 2019;106(1–2):315–31. http://dx.doi.org/10.1007/s00170-019-04565-6.

[11] Li W, Wang M, Cheng J. Indentation hardness of the cohesive-frictional materials. Int J Mech Sci 2020;180:105666. http://dx.doi.org/10.1016/j.ijmecsci.2020.105666.

[12] Hu D, Tian T, Wang X, Mao J, Xiao Z, Wang R. Surface hardening analysis for shot peened GH4720Li superalloy using a DEM-FEM coupling RV simulation method. Int J Mech Sci 2021;209:106689. http://dx.doi.org/10.1016/j.ijmecsci.2021.106689.

[13] Zhang P, Li S, Zhang Z. General relationship between strength and hardness. Mater Sci Eng A 2011;529:62–73. http://dx.doi.org/10.1016/j.msea.2011.08.061.

[14] Bowden FP, Tabor D. The area of contact between stationary and moving surfaces. Proc R Soc Lond Ser A Math Phys Sci 1939;169(938):391–413. http://dx.doi.org/10.1098/rspa.1939.0005.

[15] Bowden FP, Moore AJW, Tabor D. The ploughing and adhesion of sliding metals. J Appl Phys 1943;14(2):80–91. http://dx.doi.org/10.1063/1.1714954.

[16] Masen M, de Rooij M. Abrasive wear between rough surfaces in deep drawing. Wear 2004;256(6):639–46. http://dx.doi.org/10.1016/j.wear.2003.10.006.

[17] Ma X, de Rooij M, Schipper D. A load dependent friction model for fully plastic contact conditions. Wear 2010;269(11–12):790–6. http://dx.doi.org/10.1016/j.wear.2010.08.005.

[18] Mekicha M, de Rooij M, Jacobs L, Matthews D, Schipper D. Experimental validation of contact models for cold-rolling processes. J Mater Process Technol 2020;275:116371. http://dx.doi.org/10.1016/j.jmatprotec.2019.116371.

[19] Wilson W, Sheu S. Real area of contact and boundary friction in metal forming. Int J Mech Sci 1988;30(7):475–89. http://dx.doi.org/10.1016/0020-7403(88)90002-1.

[20] Sutcliffe M. Surface asperity deformation in metal forming processes. Int J Mech Sci 1988;30(11):847–68. http://dx.doi.org/10.1016/0020-7403(88)90010-0.

[21] Stoyanov P, Chromik RR. Scaling effects on materials tribology: from macro to micro scale. Materials 2017;10(5):550. http://dx.doi.org/10.3390/ma10050550.

[22] Decrozant-Triquenaux J, Pelcastre L, Courbon C, Prakash B, Hardell J. High temperature tribological behaviour of PVD coated tool steel and aluminium under dry and lubricated conditions. Friction 2020;9(4):802–21. http://dx.doi.org/10.1007/s40544-020-0435-7.

[23] Vellwock AE, Yao H. Biomimetic and bioinspired surface topographies as a green strategy for combating biofouling: a review. Bioinspir Biomim 2021;16(4):041003. http://dx.doi.org/10.1088/1748-3190/ac060f.

[24] Eder SJ, Grützmacher PG, Ripoll MR, Belak JF. Elucidating the onset of plasticity in sliding contacts using differential computational orientation tomography. Tribol Lett 2021;69(3). http://dx.doi.org/10.1007/s11249-021-01451-9.

[25] Hsu C-J, Stratmann A, Medina S, Jacobs G, Mücklich F, Gachot C. Does laser surface texturing really have a negative impact on the fatigue lifetime of mechanical components? Friction 2021;9(6):1766–75. http://dx.doi.org/10.1007/s40544-021-0508-2.

[26] Kutty T, Jarvis T, Ganguly C. Hot hardness and indentation creep studies on Zr–1Nb–1Sn–0.1Fe alloy. J Nucl Mater 1997;246(2–3):189–95. http://dx.doi.org/10.1016/s0022-3115(97)00108-6.

[27] Khan KB, Kutty T, Surappa M. Hot hardness and indentation creep study on Al–5% Mg alloy matrix–B4C particle reinforced composites. Mater Sci Eng A 2006;427(1–2):76–82. http://dx.doi.org/10.1016/j.msea.2006.04.015.

[28] yih Hsu C. Correlation of hot-microhardness with elevated-temperature tensile properties of low activation ferritic steel. J Nucl Mater 1986;141–143:518–22. http://dx.doi.org/10.1016/s0022-3115(86)80093-9.

[29] Atkins A, Tabor D. Hardness and deformation properties of solids at very high temperatures. Proc R Soc Lond Ser A Math Phys Sci 1966;292(1431):441–59. http://dx.doi.org/10.1098/rspa.1966.0146.

[30] Merchant HD, Murty GS, Bahadur SN, Dwivedi LT, Mehrotra Y. Hardness-temperature relationships in metals. J Mater Sci 1973;8(3):437–42. http://dx.doi.org/10.1007/bf00550166.

[31] Maugis D. Creep, hot hardness and sintering in the adhesion of metals at high temperature. Wear 1980;62(2):349–86. http://dx.doi.org/10.1016/0043-1648(80)90179-9.

[32] Suwanprateeb J. Calcium carbonate filled polyethylene: correlation of hardness and yield stress. Composites A 2000;31(4):353–9. http://dx.doi.org/10.1016/s1359-835x(99)00076-7.

[33] Cheng Y-T, Cheng C-M. Scaling, dimensional analysis, and indentation measurements. Mater Sci Eng R 2004;44(4–5):91–149. http://dx.doi.org/10.1016/j.mser.2004.05.001.

[34] Liu R, Wu XJ, Kapoor S, Yao MX, Collier R. Effects of temperature on the hardness and wear resistance of high-tungsten stellite alloys. Metall Mater Trans A 2014;46(2):587–99. http://dx.doi.org/10.1007/s11661-014-2664-8.

[35] Torres H, Varga M, Ripoll MR. High temperature hardness of steels and iron-based alloys. Mater Sci Eng A 2016;671:170–81. http://dx.doi.org/10.1016/j.msea.2016.06.058.

[36] Shisode M, Hazrati J, Mishra T, de Rooij M, van den Boogaard T. Evolution of real area of contact due to combined normal load and sub-surface straining in sheet metal. Friction 2020;9(4):840–55. http://dx.doi.org/10.1007/s40544-020-0444-6.

[37] Shisode M, Hazrati J, Mishra T, de Rooij M, ten Horn C, van Beeck J, van den Boogaard T. Modeling boundary friction of coated sheets in sheet metal forming. Tribol Int 2021;153:106554. http://dx.doi.org/10.1016/j.triboint.2020.106554.

[38] Shisode M, Hazrati J, Mishra T, de Rooij M, van den Boogaard A. Semi-analytical contact model to determine the flattening behavior of coated sheets under normal load. Tribol Int 2020;146:106–82. http://dx.doi.org/10.1016/j.triboint.2020.106182.

[39] Rudnytskyj A, Krenn S, Vorlaufer G, Gachot C. Influence of the 6061 aluminium alloy thermo-viscoplastic behaviour on the load-area relation of a contact. Materials 2021;14(6):1352. http://dx.doi.org/10.3390/ma14061352.

[40] Alamos FJ, Philo M, Go DB, Schmid SR. Asperity contact under creep conditions. Tribol Int 2021;160:107039. http://dx.doi.org/10.1016/j.triboint.2021.107039.

[41] Korzekwa D, Dawson P, Wilson W. Surface asperity deformation during sheet forming. Int J Mech Sci 1992;34(7):521–39. http://dx.doi.org/10.1016/0020-7403(92)90028-f.

[42] Bouzakis K-D, Michailidis N, Skordaris G. Hardness determination by means of a FEM-supported simulation of nanoindentation and applications in thin hard coatings. Surf Coat Technol 2005;200(1–4):867–71. http://dx.doi.org/10.1016/j.surfcoat.2005.02.122.

[43] Kumaraswamy A, Venkataraman B. Effect of temperature on constraint factor of Ti–6Al–4V under static indentation conditions. Scr Mater 2006;54(3):493–8. http://dx.doi.org/10.1016/j.scriptamat.2005.06.020.

[44] Kumaraswamy A, Rao VV. High strain-rate plastic flow behavior of Ti–6Al–4V from dynamic indentation experiments. Mater Sci Eng A 2011;528(3):1238–41. http://dx.doi.org/10.1016/j.msea.2010.10.008.

[45] Cahoon JR, Broughton WH, Kutzak AR. The determination of yield strength from hardness measurements. Metall Trans 1971;2(7):1979—1983. http://dx.doi.org/10.1007/BF02913433.

[46] Chang SC, Jahn MT, Wan CM, Lee JYM, Hsu TK. The determination of tensile properties from hardness measurements for Al-Zn-Mg alloys. J Mater Sci 1976;11(4):623–30. http://dx.doi.org/10.1007/bf01209447.

[47] Oñoro J, Salvador M, Cambronero L. High-temperature mechanical properties of aluminium alloys reinforced with boron carbide particles. Mater Sci Eng A 2009;499(1–2):421–6. http://dx.doi.org/10.1016/j.msea.2008.09.013.

[48] Narayan S, Rajeshkannan A. Hardness, tensile and impact behaviour of hot forged aluminium metal matrix composites. J Mater Res Technol 2017;6(3):213–9. http://dx.doi.org/10.1016/j.jmrt.2016.09.006.

[49] Choi Y, Park JH, Kim BM, Choi JC, Min BH. Estimation of relation between effective strain and hardness by rigid-plastic FEM. Metals Mater 2000;6(2):111–6. http://dx.doi.org/10.1007/bf03026353.

[50] Popovici V, Pavalache AC, Vasile M, Voiculescu I, Stanciu EM, Pausan D. Finite element method for simulating the vickers hardness test. Appl Mech Mater 2014;555:419–24. http://dx.doi.org/10.4028/www.scientific.net/amm.555.419.

[51] Varga M, Leroch S, Gross T, Rojacz H, Eder S, Grillenberger M, et al. Scratching aluminium alloys – Modelling and experimental assessment of damage as function of the strain rate. Wear 2021;476:203670. http://dx.doi.org/10.1016/j.wear.2021.203670.

[52] Stone D, Elmustafa AA. Analysis of indentation creep. MRS Proc 2007;1049. http://dx.doi.org/10.1557/proc-1049-aa10-02.

[53] Hamada S, Nakanishi M, Moriyama T, Noguchi H. Re-examination of correlation between hardness and tensile properties by numerical analysis. Exp Mech 2017;57(5):773–81. http://dx.doi.org/10.1007/s11340-017-0272-4.

[54] Zhang T, Jiang F, Yan L, Xu X. FEM modeling of the relationship between the high-temperature hardness and high-temperature, quasi-static compression experiment. Materials 2017;11(1):34. http://dx.doi.org/10.3390/ma11010034.

[55] Totten GE, MacKenzie DS, editors. Handbook of aluminum. CRC Press; 2003, http://dx.doi.org/10.1201/9780203912607.

[56] Rudnytskyj A, Simon P, Jech M, Gachot C. Constitutive modelling of the 6061 aluminium alloy under hot rolling conditions and large strain ranges. Mater Des 2020;190:108568. http://dx.doi.org/10.1016/j.matdes.2020.108568.

[57] Broitman E. Indentation hardness measurements at macro-, micro-, and nanoscale: a critical overview. Tribol Lett 2016;65(1). http://dx.doi.org/10.1007/s11249-016-0805-5.

[58] Zha X, Jiang F, Xu X. Investigation of modelling and stress distribution of a coating/substrate system after an indentation test. Int J Mech Sci 2017;134:1–14. http://dx.doi.org/10.1016/j.ijmecsci.2017.10.002.

[59] Varga M, Flasch M, Badisch E. Introduction of a novel tribometer especially designed for scratch, adhesion and hardness investigation up to 1000 °C. Proc Inst Mech Eng J 2016;231(4):469–78. http://dx.doi.org/10.1177/1350650115592918.

[60] Varga M, Rojacz H, Winkelmann H, Mayer H, Badisch E. Wear reducing effects and temperature dependence of tribolayer formation in harsh environment. Tribol Int 2013;65:190–9. http://dx.doi.org/10.1016/j.triboint.2013.03.003.

[61] Endo T, Masuyama F, Park K-S. Change in vickers hardness and substructure during creep of a mod.9cr-1mo steel. Mater Trans 2003;44(2):239–46. http://dx.doi.org/10.2320/matertrans.44.239.

[62] Choi I-C, Yoo B-G, Kim Y-J, il Jang J. Indentation creep revisited. J Mater Res 2011;27(1):3–11. http://dx.doi.org/10.1557/jmr.2011.213.

[63] Zener C, Hollomon JH. Effect of strain rate upon plastic flow of steel. J Appl Phys 1944;15(1):22–32. http://dx.doi.org/10.1063/1.1707363.

[64] Garofalo F. Fundamentals of creep and creep-rupture in metals. Macmillan; 1965, p. 258, URL https://archive.org/details/fundamentalsofcr0000garo.

[65] Sellars C, McTegart W. On the mechanism of hot deformation. Acta Metall 1966;14(9):1136–8. http://dx.doi.org/10.1016/0001-6160(66)90207-0.

[66] Wang X, Jiang F, Zhang T, Wang L. Study on dynamic mechanical properties and constitutive model of 10B/Al composite compared with its matrix of high-purity aluminum. J Mater Sci 2019;55(2):748–61. http://dx.doi.org/10.1007/s10853-019-03949-z.

[67] Mehtedi ME, Spigarelli S, Gabrielli F, Donati L. Comparison study of constitutive models in predicting the hot deformation behavior of AA6060 and AA6063 aluminium alloys. Mater Today: Proc 2015;2(10):4732–9. http://dx.doi.org/10.1016/j.matpr.2015.10.006.

[68] Spigarelli S, Mehtedi ME. A new constitutive model for the plastic flow of metals at elevated temperatures. J Mater Eng Perform 2013;23(2):658–65. http://dx.doi.org/10.1007/s11665-013-0779-5.

[69] Lin Y, Chen X-M. A critical review of experimental results and constitutive descriptions for metals and alloys in hot working. Mater Des 2011;32(4):1733–59. http://dx.doi.org/10.1016/j.matdes.2010.11.048.

[70] Muzyka NR. Influence of the anisotropy of sheet materials on the accuracy of measuring of the Vickers hardness. Strength Mater 2007;39(2):211–8. http://dx.doi.org/10.1007/s11223-007-0027-z.

[71] Vaidya N, Joshi MJ, Shah BS, Joshi DR. Knoop hardness anisotropy in anthracene and phenanthrene single crystals. Bull Mater Sci 1997;20(8):1103–8. http://dx.doi.org/10.1007/bf02745062.

[72] ASM. Properties and selection: nonferrous alloys and special-purpose materials. ASM International; 1990, http://dx.doi.org/10.31399/asm.hb.v02.9781627081627.

[73] Poisl W, Oliver W, Fabes B. The relationship between indentation and uniaxial creep in amorphous selenium. J Mater Res 1995;10(8):2024–32. http://dx.doi.org/10.1557/jmr.1995.2024.

[74] Baral P, Kermouche G, Guillonneau G, Tiphene G, Bergheau J-M, Oliver WC, et al. Indentation creep vs. indentation relaxation: A matter of strain rate definition? Mater Sci Eng A 2020;781:139246. http://dx.doi.org/10.1016/j.msea.2020.139246.

[75] Guo B, Zhang L, Cao L, Zhang T, Jiang F, Yan L. The correction of temperature-dependent Vickers hardness of cemented carbide base on the developed high-temperature hardness tester. J Mater Process Technol 2018;255:426–33. http://dx.doi.org/10.1016/j.jmatprotec.2017.12.041.

[76] Virtanen P, Gommers R, Oliphant TE, Haberland M, Reddy T, Cournapeau D, et al. SciPy 1.0: fundamental algorithms for scientific computing in python. Nature Methods 2020;17:261–72. http://dx.doi.org/10.1038/s41592-019-0686-2.

[77] Hunter JD. Matplotlib: A 2D graphics environment. Comput Sci Eng 2007;9(3):90–5. http://dx.doi.org/10.1109/MCSE.2007.55.

[78] Ramachandran P, Varoquaux G. Mayavi: 3D visualization of scientific data. Comput Sci Eng 2011;13(2):40–51.

[79] Slooff F, Zhou J, Duszczyk J, Katgerman L. Constitutive analysis of wrought magnesium alloy Mg–Al4–Zn1. Scr Mater 2007;57(8):759–62. http://dx.doi.org/10.1016/j.scriptamat.2007.06.023.